

NONPARAMETRIC TESTS OF STRUCTURE FOR HIGH ANGULAR RESOLUTION DIFFUSION IMAGING IN Q -SPACE¹

BY SOFIA C. OLHEDE AND BRANDON WHITCHER

University College London and GlaxoSmithKline

High angular resolution diffusion imaging data is the observed characteristic function for the local diffusion of water molecules in tissue. This data is used to infer structural information in brain imaging. Nonparametric scalar measures are proposed to summarize such data, and to locally characterize spatial features of the diffusion probability density function (PDF), relying on the geometry of the characteristic function. Summary statistics are defined so that their distributions are, to first-order, both independent of nuisance parameters and also analytically tractable. The dominant direction of the diffusion at a spatial location (voxel) is determined, and a new set of axes are introduced in Fourier space. Variation quantified in these axes determines the local spatial properties of the diffusion density. Nonparametric hypothesis tests for determining whether the diffusion is unimodal, isotropic or multi-modal are proposed. More subtle characteristics of white-matter microstructure, such as the degree of anisotropy of the PDF and symmetry compared with a variety of asymmetric PDF alternatives, may be ascertained directly in the Fourier domain without parametric assumptions on the form of the diffusion PDF. We simulate a set of diffusion processes and characterize their local properties using the newly introduced summaries. We show how complex white-matter structures across multiple voxels exhibit clear ellipsoidal and asymmetric structure in simulation, and assess the performance of the statistics in clinically-acquired magnetic resonance imaging data.

1. Introduction. Many applications in brain imaging are based on calculating local statistics that are later combined to infer global properties of spatial links or functional connections. In this paper we focus on the local analysis of high angular resolution diffusion imaging (HARDI) data,

Received June 2010; revised October 2010.

¹Supported by EPSRC and GlaxoSmithKline via EP/E031536/1.

Key words and phrases. Anisotropy, asymmetry, magnetic resonance imaging, diffusion weighted imaging, nonparametric.

<p>This is an electronic reprint of the original article published by the Institute of Mathematical Statistics in <i>The Annals of Applied Statistics</i>, 2011, Vol. 5, No. 2B, 1293–1327. This reprint differs from the original in pagination and typographic detail.</p>
--

a special type of magnetic resonance imaging (MRI). HARDI observations correspond to the local (in a single voxel²) measurement of the local molecular diffusion of water at a number of different orientations over a spherical shell of fixed radius [Callaghan (1993)]. Measurements from an MRI scanner are taken directly in the Fourier domain and translated into the spatial domain via the inverse Fourier transform.

A HARDI acquisition scheme permits the characterization of directional spatial properties of the diffusion probability density function (PDF). The local structure of white-matter brain tissue may be inferred from such measurements [Basser, Mattiello and Bihan (1994); Basser (2002)]. Once local statistics have been formed, it is of interest to combine information across voxels (spatial locations), for example, to connect local directions of estimated diffusion PDFs to recognize major nerve fiber tracts, to infer local fiber structure from the estimated diffusions [Mori and van Zijl (2002)], and/or to use other locally-defined statistical summaries in inferential procedures [Jensen et al. (2005)].

Different orientational sampling designs can be used at each voxel and, if a simple parametric model is used for the PDF, then rather sparse sampling will be sufficient to recover the parameters of the model. Traditional analysis of HARDI measurements is based on modeling the diffusion PDF parametrically as a (zero-mean) Gaussian, and estimating a diffusion tensor (the covariance matrix of the Gaussian PDF), a procedure which corresponds to diffusion tensor imaging (DTI). Such methods have drawbacks, namely, of not describing more complex white-matter structures well, and their usage trades a small variance for potentially large bias. While the diffusion tensor model has both theoretical justification—and has been extremely popular—it prohibits one from describing more complicated white-matter microstructure, such as crossing, kissing and forking fibers [Mori and van Zijl (2002)].

It is believed that intravoxel orientational heterogeneity affects as many as one third of all imaged white-matter voxels [Behrens et al. (2007)], and so addressing such structure is important. With more time-intensive sampling schemes (such as HARDI [Tuch et al. (2002)] or diffusion spectrum imaging), the possibility of more complicated estimators may be used, for example, multi-tensor modeling [Alexander (2005)], nonparametric alternatives such as persistent angular structure MRI [Jansons and Alexander (2003)], Q -ball imaging [Tuch (2004)], the diffusion orientation transform [Özarslan et al. (2006)] and spherical deconvolution [Tournier et al. (2004)]. While using a nonparametric approach removes bias, usage of such nonparametric methods is challenging because the diffusion process is measured in the

²A voxel is a three-dimensional “volume element” of data, just as a pixel is a two-dimensional “area element” of data.

Fourier domain (q -space³), and the characteristic function has been considerably undersampled to accommodate realistic scanning times in practice. This challenges the stable inversion of information, the local characteristic function, to local spatial structure.

This paper develops a statistical framework, using nonparametric methods, for characterizing HARDI data directly in q -space [Tuch et al. (2002)] without local inversion. This avoids calculating nonlinear transformations of the data, whose usage usually leads to intractability of the distributions of statistical summaries. The approximate distributions of the proposed estimators in this paper are derived and are defined so that, to first order, they are free of any nuisance parameters. The proposed statistics are a first step toward the automated detection of subtle characteristics of white-matter microstructure, that is, scalene diffusions (Figure 1) or asymmetry in decay in a fixed axis. Both properties, scalene diffusion and asymmetry, have been found in a forking fiber structure (Figure 1), and may be important summaries to feed into fiber-tracking algorithms [Mori and van Zijl (2002)]. The derived methods also serve as a warning when interpreting multi-tensor models in clinically-feasible acquisition schemes, as similar characteristics can be obtained from more complex single peaked structures.

Global features like bi- or multi-modality of the diffusion PDF are described reasonably well by many methods over a range of signal-to-noise ratios (SNRs), with the small caveat that the various implicit assumptions inherent to any of the given methods must be satisfied. Parametric models introduce bias when they are not appropriate, whereas using a nonparametric method increases the variance in the estimation. Using a moderate number of directions in the HARDI sampling scheme restricts the possibility of determining smaller scale structure of the diffusion PDF. Strong parametric assumptions increase the power of any proposed statistic to detect multiple diffusion directions, with the consequence that any deviation from the prescribed structure in the parametric model may be used to reject null hypotheses such as unimodality.

In the method proposed here to determine the properties of the diffusion PDF, prolate diffusion PDFs are separated from isotropic (or spherical) PDFs using a test based on a comparison of relative magnitudes in q -space; see Figure 1 for illustrations of prolate and spherical diffusion models. Subsequently, multi-modal distributions are then differentiated from the isotropic and unidirectional. The unidirectional diffusion is associated with

³ Q -space is the Fourier domain representation of the local diffusion and is the space where measurements are made in MRI. The global image Fourier representation is usually inverted to a spatial representation, but the local Fourier transform is not inverted as part of the acquisition, leaving the spatial domain observations associated with a measurement of local diffusion in a Fourier domain orientation.

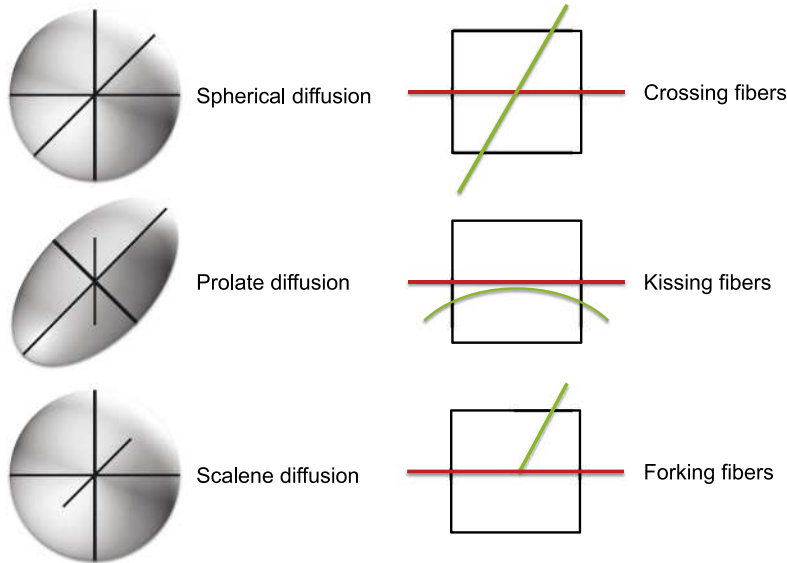


FIG. 1. *Simplified diagrams for typical Gaussian diffusion models (first column) and fiber configurations in a voxel of white matter in the brain (second column). Spherical diffusion is found when no fibers are present in a voxel of brain tissue (e.g., cerebral-spinal fluid) and all eigenvalues are equal ($\lambda_1 = \lambda_2 = \lambda_3$). Prolate diffusion is when a single fiber bundle is present in the voxel ($\lambda_1 \gg \lambda_2 = \lambda_3$). Scalene diffusion is when two fiber bundles of similar mass cross in perpendicular directions ($\lambda_1 \approx \lambda_2 \gg \lambda_3$). The concept of “crossing fibers” involves two fiber bundles that do not necessarily intersect at right angles in the same voxel. The concept of “kissing fibers” involves two fiber bundles that occupy the same voxel, but do not intersect. The concept of “forking fibers” involves a single fiber going in the voxel and two fiber bundles leaving the voxel. A “fanning fiber” (not shown) is similar to a forking fiber, but instead of a single direction the fiber produces multiple diverging fibers on one side of the voxel.*

a great circle in q -space [Tuch (2004)], and we call this the *dominant great circle*. The strongest direction defines an important spatial summary of the diffusion PDF, and specifies the major axis of the diffusion in q -space (Figure 2g). The perpendicular to the major direction in space defines a set of points lying on a great circle in q -space, which exactly corresponds to the dominant great circle.

If a given voxel has been diagnosed as unidirectional (or if there is a dominant great circle in q -space), then we seek to characterize its main unidirectional structure in more detail. A scalar measure resembling the popular fractional anisotropy⁴ is defined as the *anisotropy statistic*, by comparing the

⁴The fractional anisotropy (FA) is a measure of uniformity of the eigenvalues of a Gaussian covariance matrix [Basser and Pierpaoli (1996)].

magnitude of the q -space diffusion on the dominant great circle with its two perpendicular point(s). This measure determines the degree of anisotropy of the diffusion PDF. Further investigation of unidirectional voxels causes us to focus on quantifying the uniformity of decay in the minor axes of the diffusion PDF, or the perpendicular to the dominant great circle, to describe further detailed structure of the characteristic function.

Ellipsoidal diffusions are an important class of diffusions and the scalene structure of the diffusion PDF is particularly important when combining voxel-wise information [Seunarine et al. (2007)]. The aforementioned work showed that the scalene structure of the peak is related to the peak anisotropy in space and important for treating bending and fanning fibers (Figure 1). For diffusions with ellipsoidal decay, their minor axes are well defined by this (scalene) decay structure, while for nonellipsoidal diffusions the minor axes correspond to a set of axes in the plane of the dominant great circle, parameterizing locations on the dominant great circle. We examine the scalene structure of the diffusion PDF, which is quantified by the difference in decay in the two spatial minor axes, defined as such also for nonellipsoid diffusions. This corresponds to examining the variability of the diffusion on the great circle perpendicular to the vector associated with the major direction of the diffusion. For a Gaussian diffusion model this is given by the two minor eigenvalues of the eigen-decomposition of the diffusion tensor. A statistical test for uniformity on the great circle is developed that can be related to the spatial decay of the diffusion PDF in the minor axes. Another feature of interest in the PDF is asymmetry in the decay in a fixed direction perpendicular to the dominant great circle. This heuristic may be visualized in space as a diffusion PDF that appears ellipsoidal but the peak is in one of the foci rather than the center of the ellipse. We introduce a test statistic for asymmetry based on this understanding. To motivate our interest in asymmetry and ellipsoidality, we simulate forking and crossing structures, and show how both asymmetry and ellipsoidality follow as precursors to forking structure, and such information could be used to improve the tracking of fibers.

The methodology presented here improves our understanding of the diffusion PDF by not relying on parametric assumptions when analyzing the measurements, yet still relating q -space structure directly to spatial properties. Nonparametric statistical summaries are defined directly in q -space to increase the power of the proposed hypothesis tests and theoretical critical values for the statistics are provided. Understanding the inherent limitations of HARDI measurements can be obtained directly from our discussion of simulated diffusions, thus increasing the understanding of parametric assumptions that are necessary to derive more complicated structures from the diffusion PDF.

2. Statistical models for HARDI data.

2.1. *Observational model.* We denote the sampling of the observations by the set $\mathcal{Q}_0 = \{\tilde{\mathbf{q}}_i\}_{i=1}^n$. At each $\tilde{\mathbf{q}}_i = (\tilde{q}_{i1}, \tilde{q}_{i2}, \tilde{q}_{i3})$ on the unit sphere $\|\tilde{\mathbf{q}}\| = (\tilde{q}_1^2 + \tilde{q}_2^2 + \tilde{q}_3^2)^{1/2} = 1$ we obtain an observed measurement $\tilde{A}(\tilde{\mathbf{q}}_i) \geq 0$, corresponding to the magnitude of a complex-valued observation (proportional to the noisy characteristic function of local diffusion⁵). Furthermore, we take n_0 observations at $\mathbf{q} = \mathbf{0}$, denoted by $\tilde{A}_k(\mathbf{0})$ for $k = 1, \dots, n_0$. We distinguish here between the measured apparent diffusion at $\tilde{\mathbf{q}}_i$, namely, $\tilde{A}(\tilde{\mathbf{q}}_i)$, and the theoretical diffusion value, $\mathcal{A}(\tilde{\mathbf{q}}_i)$. Note that the expected value of $\tilde{A}(\tilde{\mathbf{q}}_i)$ is *not* equivalent to $\mathcal{A}(\tilde{\mathbf{q}}_i)$, for two reasons. First because the observations are magnitudes, with the noise contributing in the expectation, and second we need to re-normalize the observed diffusion to have unit volume, as noted by Alexander (2005). As the PDF is a density, it has to satisfy the normalization of

$$(2.1) \quad \iiint a(\mathbf{x}) d^3 \mathbf{x} = 1 \quad \Rightarrow \quad \mathcal{A}(\mathbf{0}) = 1,$$

where $a(\mathbf{x})$ is the diffusion probability density function (PDF), or the inverse Fourier Transform of $\mathcal{A}(\mathbf{q})$. We apply a biased estimator of a simple average to estimate the inverse of the normalizing constant by $\bar{A}(\mathbf{0}) = n_0^{-1} \sum_{k=1}^{n_0} \tilde{A}_k(\mathbf{0})$. We re-normalize the observed diffusion such that $A(\tilde{\mathbf{q}}_i) = \tilde{A}(\tilde{\mathbf{q}}_i) / \bar{A}(\mathbf{0})$. The diffusion value $A(\tilde{\mathbf{q}}_i)$ has (approximately) a Rician distribution with parameters $\mathcal{A}(\tilde{\mathbf{q}}_i)$ and σ^2 [Gudbjartsson and Patz (1995)]. As the SNR will be large at $\mathbf{q} = \mathbf{0}$, the noise floor of the Rician distribution will have limited impact in the estimation of the normalization constant. While the diffusion PDF $a(\mathbf{x})$ is not Gaussian, the Rician distribution under reasonable SNR is well approximated by the Gaussian, and sums of Rician variables will be very similar to a Gaussian. In subsequent sections we shall calculate statistical estimators from normalized measurements $\{A(\tilde{\mathbf{q}}_i)\}_i^n$ and look at maxima of these statistics, which may be represented (approximately) by the maxima of suitably-scaled Gaussian random variables. If we are in the regime of low SNR, then these test statistics will be approximated by a mixture of Gaussian and Chi random variables whose tail-behavior is not substantially heavier than Gaussian random variables, but whose mean is not consistent with our results. An assumption for the method to work is therefore a reasonable level of the SNR, as is further discussed in Section 5.

The normalized diffusion measurements $\mathcal{A}(\tilde{\mathbf{q}}_i)$ should exhibit symmetry as the diffusion PDF is real-valued, symmetric and indeed positive,

⁵Note that this is different from the empirical characteristic function.

that is, $\mathcal{A}(-\tilde{\mathbf{q}}_i) = \mathcal{A}(\tilde{\mathbf{q}}_i)$ [Wedeen et al. (2005)]. To fully exploit the Hermitian symmetry, we shall reflect the observations to the augmented set $\mathcal{Q} = \{\mathbf{q}: \mathbf{q} \in \mathcal{Q}_0\} \cup \{\mathbf{q}: -\mathbf{q} \in \mathcal{Q}_0\}$, and set $A(-\tilde{\mathbf{q}}_i) = A(\tilde{\mathbf{q}}_i)$ [Jansons and Alexander (2003)].

We assume that a nonparametric estimator of the diffusion in q -space is constructed. For our purposes we have chosen to use a variable-bandwidth estimator [Olhede and Whitcher (2008a, 2008b)], but the methodology outlined here is applicable to other linear estimators (e.g., radial basis functions and/or spherical harmonics) with some straightforward alteration of the statistical properties (specifically, second-order structure) of the estimators.

2.2. Great circles in q -space. Spatial properties of the diffusion PDF may be described directly in q -space. The advantage of such an operation is that we avoid the need to invert the PDF to the spatial domain for analysis, allowing us to employ a broad range of modeling approaches. A basic building block of our analysis is an *ellipsoid density*. We refer to a density $a_E(\mathbf{x})$ as an ellipsoid density if its FT takes the form

$$(2.2) \quad \mathcal{A}_E(\mathbf{q}; \mathbf{\Lambda}, \mathbf{\Upsilon}) = B\left(\sqrt{\sum_{j=1}^3 \lambda_j |\mathbf{v}_j^T \mathbf{q}|^2}\right),$$

where $\lambda_j \geq 0$ for $j = 1, 2, 3$, $\{\mathbf{v}_j\}$ constitutes a basis for \mathbb{R}^3 and $B(\cdot)$ is a monotonically decreasing function. For example, it is common to use the Gaussian characteristic function $B(q) = e^{-2(\pi q)^2}$. We collect the eigenvalues in the matrix $\mathbf{\Lambda} = \text{diag}(\lambda_1, \lambda_2, \lambda_3)$, and define

$$(2.3) \quad \mathbf{\Upsilon}^T = \begin{bmatrix} v_{11} & v_{12} & v_{13} \\ v_{21} & v_{22} & v_{23} \\ v_{31} & v_{32} & v_{33}, \end{bmatrix}$$

to model the axis of any orientational structure. Ellipsoid densities are natural building blocks, just like the special case of the DTI model, but do not (for example) include multi-modal densities. If the q -space density takes this form, then the spatial PDF is given by inverting the FT

$$(2.4) \quad a_E(\mathbf{x}; \mathbf{\Lambda}, \mathbf{\Upsilon}) = \iiint_{\mathbb{R}^3} \mathcal{A}_E(\mathbf{q}; \mathbf{\Lambda}, \mathbf{\Upsilon}) e^{i2\pi \mathbf{q}^T \mathbf{x}} d^3 \mathbf{q}$$

[Callaghan (1993)]. We note for $\mathbf{x} \in \mathbb{R}^3$, with $x = \|\mathbf{x}\|$ and $q = \|\mathbf{q}\|$, that $a_E(\mathbf{x}; \mathbf{\Lambda}, \mathbf{\Upsilon})$ takes the form

$$(2.5) \quad a_E(\mathbf{x}; \mathbf{\Lambda}, \mathbf{\Upsilon}) = |\mathbf{\Lambda}|^{1/2} b(\|\mathbf{\Lambda}^{-1/2} \mathbf{\Upsilon} \mathbf{x}\|),$$

where

$$(2.6) \quad b(x) = \int_{-\infty}^{\infty} \int_{-\infty}^{\infty} \int_{-\infty}^{\infty} B(q) e^{i2\pi \mathbf{q}^T \mathbf{x}} d^3 \mathbf{q}$$

$$(2.7) \quad = \frac{1}{2\pi^2 x} \int_0^{\infty} B\left(\frac{q'}{2\pi}\right) \sin(xq') q' dq'$$

$$(2.8) \quad = \frac{2}{x} \int_0^{\infty} B(q) \sin(2\pi xq) q dq,$$

which follows from Gradshteyn and Ryzhik (2000), page 1112. The meaning of “ellipsoid density” becomes clear from this expression, since whenever $\|\mathbf{\Lambda}^{-1/2} \mathbf{\Upsilon} \mathbf{x}\| = R$, where $R \geq 0$ is a constant, the function $a_E(\mathbf{x})$ takes the same value in space. As long as all the eigenvalues are positive, $a_E(\cdot)$ will map out ellipsoidal contours of equal function value in space. The Gaussian DTI model fits into this class of densities with $b(x) = (2\pi)^{-3/2} e^{-x^2/2}$ as well as, for example, the Matérn family with the spatial variable exchanged with the spatial-frequency variable [Matérn (1960)]. The model proposed by Kaden, Knösche and Anwender (2007) is also related to such densities.

Figure 2 provides examples of diffusion processes displayed in both the spatial and frequency (q -space) domains. The spatial domain corresponds to the diffusion PDF, whereas its Fourier transform corresponds to the q -space representation. Common processes, such as prolate and scalene diffusion, are given as well as more exotic examples, such as a mixture of prolate diffusion processes and a process that cannot be represented using a Gaussian diffusion model. The values of $\mathbf{\Upsilon}$ specify the orientation of the diffusion PDF, while $\mathbf{\Lambda}$ gives its qualitative appearance when coupled with $B(\cdot)$. Looking directly at Figure 2, it may be difficult for one to appreciate the local structure near the peak, which motivates us to develop a new class of statistics to characterize the diffusion PDF.

2.3. *The orientation distribution function.* An important tool in understanding HARDI data is the orientational distribution function (ODF). The ODF quantifies the directional structure of the diffusion PDF in space. A popular object of study, it corresponds to several different functions in the literature. Tuch (2004) and Hess et al. (2006); Descoteaux et al. (2007) define the ODF to be

$$(2.9) \quad \text{ODF}_T(\theta, \phi) = \frac{1}{Z} \int_0^{\infty} a(r \mathbf{u}) dr,$$

where $\mathbf{x} = r \mathbf{u}$, $\|\mathbf{u}\| = 1$ and Z is a normalizing constant. Because this is not a true marginalization of a PDF (the increment needs a weighting by r^2), and weights lower scales heavily, the diffuse directional structure of the large-scale structure smooths the marginal PDF of orientations, giving it

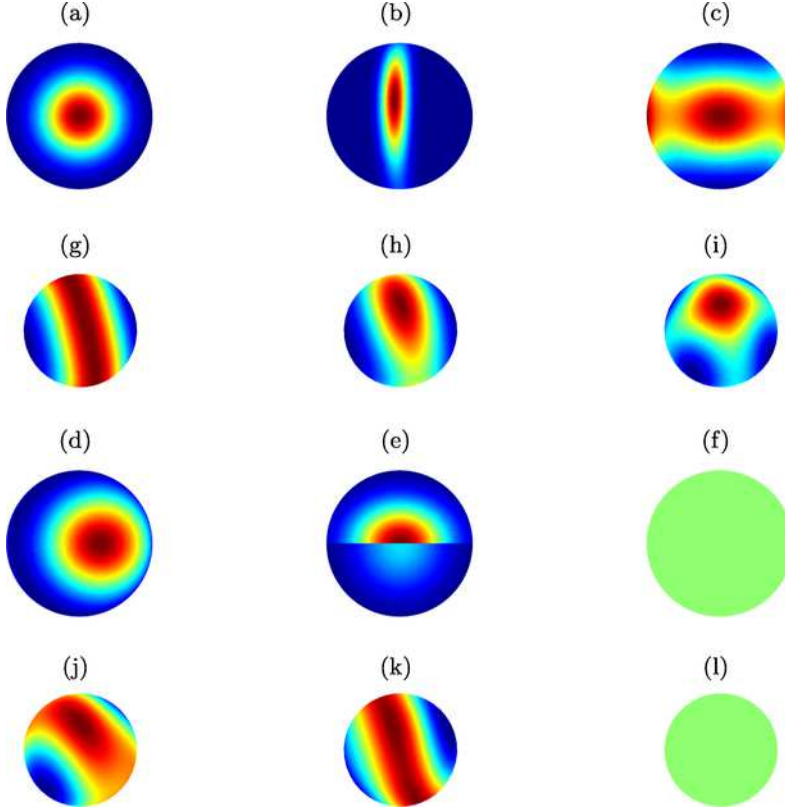


FIG. 2. Diffusion processes displayed in both spatial and frequency (q -space) domains, with coloring representing density on the sphere. Ellipsoid diffusions are represented by their covariance matrix eigenvalues $\{\lambda_i\}_{i=1}^3$ which govern a symmetric spatial decay. (a, g) Prolate (ellipsoid) diffusion process ($\lambda_1 \gg \lambda_2 = \lambda_3$). A prolate diffusion process is dominated by a single direction, represented by (a) a single peak in the diffusion PDF and (g) a great circle perpendicular to the diffusion direction in q -space. (b, h) Scalone (ellipsoid) diffusion process ($\lambda_1 \approx \lambda_2 \gg \lambda_3$). A scalene diffusion process has two competing directions, which makes the minor axes unequally matched in both spaces. (c, i) A mixture of prolate (ellipsoid) diffusions. This cannot be represented by a single unimodal diffusion PDF but must be represented by two directions. (d, j) and (e, k) These are both (nonellipsoid appearing) diffusion PDFs with asymmetric structure, suitable to model precursors to branching or forking (see text). Neither of these diffusion PDFs can be thought of as ellipsoid. (f, l) Isotropic diffusion with no directional structure in space or q -space.

a “blunted” appearance. A nonlinear transformation is necessary for the ODF to have a more peaked and clear directional structure. Wedeen et al. (2005) define the ODF as the truly marginalized PDF over all spatial radii

$$(2.10) \quad \text{ODF}_W(\theta, \phi) = \int_0^\infty r^2 a(r\mathbf{u}) dr.$$

An alternative version may be found in Jansons and Alexander (2003), where the orientational structure associated with a single radius is fitted to the observed data, that is, the persistent angular structure (PAS-MRI) algorithm. It is useful to note that the observed data are not associated purely with a single radius, and for this to be a mathematically correct procedure the observed HARDI measurements should be convolved with a suitable kernel prior to estimation. Despite this fact, the PAS-MRI method usually produces good results in practice. All three of these orientational summaries are measuring different properties of the directional structure of the data, and only $\text{ODF}_W(\cdot, \cdot)$ is a true marginal PDF.

Another directional representation of diffusion data corresponds to the spherical convolution model [Tournier et al. (2004)]. In this model, q -space observations are modeled as convolved fiber ODFs, and fiber populations are estimated using deconvolution methods. The magnitudes are not comparable with previously-defined estimators of ODFs. Extensions to these methods have also been proposed: by modeling the ODF as a mixture of Bingham distributions [Kaden, Knösche and Anwender (2007)], and by regularizing the deconvolution problem by applying constrained optimization methods [Jian and Vemuri (2007)]. The solution in Kaden, Knösche and Anwender (2007) is parametric and the theoretical assumptions necessary to apply the regularized methods are, in general, violated [Jian and Vemuri (2007)].

The ellipsoid diffusion model (2.5) may be extended into a larger class of arbitrarily peaked and deformed diffusion PDFs by taking

$$(2.11) \quad \mathbf{\Lambda}(\mathbf{x}) = \text{diag}(\lambda_{11}(\mathbf{x}), \lambda_{22}(\mathbf{x}), \lambda_{33}(\mathbf{x})), \quad \lambda_{jj}(\mathbf{x}) \geq 0 \forall \mathbf{x},$$

with C a normalizing constant, to produce the diffusion PDF

$$(2.12) \quad a_{\text{DE}}(\mathbf{x}) = C \sqrt{|\mathbf{\Lambda}(\mathbf{\Upsilon}\mathbf{x})|} b(\|\mathbf{\Lambda}(\mathbf{\Upsilon}\mathbf{x})^{-1/2}\mathbf{\Upsilon}\mathbf{x}\|),$$

$$(2.13) \quad a_{\text{DE}}(\mathbf{\Upsilon}^T \mathbf{x}) = C \sqrt{|\mathbf{\Lambda}(\mathbf{x})|} b(\|\mathbf{\Lambda}(\mathbf{x})^{-1/2}\mathbf{x}\|).$$

Because $\mathbf{\Lambda}(\mathbf{x})$ is a diagonal matrix, $a_{\text{DE}}(\mathbf{\Upsilon}^T \mathbf{x})$ exhibits the axes $(1, 0, 0)$, $(0, 1, 0)$ and $(0, 0, 1)$. Applying a Fourier transform directly, with a change of variables, we note that the Fourier transform is mixed over the strengths in $\mathbf{\Lambda}(\mathbf{x})$, but exhibits the same orientational axes if the ordering in magnitude of the eigenvalues does not switch over \mathbf{x} . We have the model of

$$(2.14) \quad \mathcal{A}_{\text{DE}}(\mathbf{q}) = C \iiint_{\mathbb{R}^3} |\mathbf{\Lambda}(\mathbf{x})|^{1/2} b(\|\mathbf{\Lambda}(\mathbf{x})^{-1/2}\mathbf{x}\|) e^{-i2\pi(\mathbf{\Upsilon}\mathbf{q})^T \mathbf{x}} d^3\mathbf{x}.$$

This function can take the appearance of a deformed ellipsoid in space, and may then exhibit a different pattern of decay to the left and right of the dominant great circle in q -space. For the regular ellipsoid distribution $a_{\text{E}}(\mathbf{x})$ if one eigenvalue is larger than the two others (say, $\lambda_1 > \lambda_2 \geq \lambda_3$),

then the ellipsoid density [or equally in the case of the deformed density if $\inf_{\mathbf{x}} \lambda_1(\mathbf{x}) > \sup_{\mathbf{x}} \lambda_2(\mathbf{x})$] will observe a maximum at the values

$$(2.15) \quad \mathbf{q}(\beta) = \begin{cases} \beta \mathbf{v}_2 + \sqrt{1 - \beta^2} \mathbf{v}_3, & \text{if } \beta \in [-1, 1], \\ \text{sgn}(\beta)(2 - |\beta|) \mathbf{v}_2 \\ \quad - \sqrt{1 - (2 - |\beta|)^2} \mathbf{v}_3, & \text{if } \beta \in [-2, -1] \cup [1, 2]. \end{cases}$$

Figure 2g and h help to illustrate the behavior of (2.15), where the location on the ‘‘belt’’ is given by the value of β . Note, the diffusion PDFs have been rotated in space compared to each other for a better visual perspective. The maximum great circle in q -space corresponds to the perpendicular vector $\pm \mathbf{v}_1$ in space, where the diffusion PDF exhibits a maximum. The structure near the peak ($\mathbf{x} = \pm \mathbf{v}_1$) is mapped to a structure contiguous to the great circle, that is, $\mathbf{q} \approx \mathbf{q}(\beta)$. Comparing the unimodal diffusion models (in Figure 2a, b and d), the microstructure of the diffusion PDF is mapped into behavior near or on the belt $\mathbf{q}(\beta)$; see Figure 2g, h and j. The scale structure of the diffusion PDF corresponds to variation on the belt (Figure 2h), while the asymmetry of Figure 2d and e are mapped onto the local structure of the delineation of the belt in Figure 2j and k. This motivates us to investigate the structure of the diffusion PDF near the great circle of points $\{\mathbf{q}(\beta)\}$ using distances from the great circle to characterize structure in the decay from the main peak. To obtain consistency in notation, we define the set of points, or the great circle perpendicular to \mathbf{v} , via $\mathcal{G}(\mathbf{v}) = \{\mathbf{q} : \mathbf{v}^T \mathbf{q} = 0, \|\mathbf{q}\| = 1\}$ and $\mathcal{G}(\mathbf{v}_1) \equiv \{\mathbf{q}(\beta)\}$. It is convenient to keep both sets of notation for ease of exposition in the future.

3. Scalar summaries and test statistics.

3.1. *Axes of symmetry.* Before we can define appropriate scalar summaries in q -space, additional axes to the β axis (2.15) are required. For any fixed vector $\mathbf{q}(\beta) \in \mathcal{G}(\mathbf{v}_1)$ we traverse a great circle using the vectors

$$(3.1) \quad \mathbf{q}_{\perp}(\alpha, \beta) = \alpha \mathbf{v}_1 \pm \sqrt{1 - \alpha^2} \mathbf{q}(\beta), \quad \alpha \in [-1, 1],$$

where for $\alpha \in [-2, 2] \setminus [-1, 1]$, the corresponding expression may be formed as in (2.15). Such a great circle for a fixed value of β will be referred to as a *perpendicular great circle*.

An important component in the definition of our nonparametric summaries is the *dominant great circle* $\mathcal{G}(\mathbf{x}_{\max})$ with \mathbf{x}_{\max} given by

$$(3.2) \quad \mathbf{x}_{\max} = \arg \max_{\mathbf{v}} \left\{ \oint_{\mathbf{q} \in \mathcal{G}(\mathbf{v})} \mathcal{A}(\mathbf{q}) d\mathbf{q} \right\}.$$

If $\mathcal{A}(\mathbf{q})$ is an isotropic diffusion process, then \mathbf{x}_{\max} is any vector in \mathbb{R}^3 with a fixed norm. Alternatively, if $\mathcal{A}(\mathbf{q})$ is ellipsoid with $\lambda_1 > \lambda_2 \geq \lambda_3$, then

$\mathbf{x}_{\max} = \mathbf{v}_1$. If there are two fibers, with relative weights of a_1 and a_2 of fiber populations with individual eigenvalues $\mathbf{\Lambda}^{(1)}$ and $\mathbf{\Lambda}^{(2)}$, then

$$(3.3) \quad \mathbf{x}_{\max} = \arg \max_{\mathbf{v}} \left\{ \left[a_1 \oint_{\mathbf{q} \in \mathcal{G}(\mathbf{v})} \mathcal{A}_E(\mathbf{q}; \mathbf{\Lambda}^{(1)}, \mathbf{\Upsilon}^{(1)}) + a_2 \oint_{\mathbf{q} \in \mathcal{G}(\mathbf{v})} \mathcal{A}_E(\mathbf{q}; \mathbf{\Lambda}^{(2)}, \mathbf{\Upsilon}^{(2)}) \right] d\mathbf{q} \right\}.$$

For example, if $a_1 \gg a_2$, then $\mathbf{x}_{\max} \approx \mathbf{v}_1^{(1)}$, or if $a_1 = a_2 = 1/2$ and the great circles do not separate, then \mathbf{x}_{\max} will lie precisely between the two maxima of the two diffusion PDFs. Once the great circles start to separate the maximum will go with one of the two.

3.2. Degree of nonuniformity. We represent a unidirectional Gaussian diffusion by plotting the value of $\mathcal{A}(\mathbf{q}(\beta))$ (solid line) for $\beta \in [-2, 2]$ in Figure 3a. The magnitude on the dominant great circle is constant over different values of β since $\lambda_2 = \lambda_3$. To illustrate the difference in variation across the dominant and perpendicular great circles, we also plot the value of $\mathcal{A}(\mathbf{q}_{\perp}(\alpha, \beta))$ as a function of α for a fixed β (dotted line). This line perfectly overlaps $\mathcal{A}(\mathbf{q}(\beta))$ at two locations, as it collides with the dominant great circle when it wraps around the sphere, and decays symmetrically from $\mathbf{q}(\beta)$.

We define a new coordinate system (α, β) , where we expect consistent variability in α and β , using our parameterization of great circles (3.1). We plot the unidirectional Gaussian diffusion $\mathcal{A}(\mathbf{q}_{\perp}(\alpha, \beta))$ for all perpendicular great circles in the plane (Figure 3b). This prolate diffusion exhibits variation only in α , which is variation perpendicular to the dominant great circle. For the prolate diffusion example we can therefore reduce the variance by averaging across β and by considering the function strictly in terms of α . For comparison with the (α, β) plane, the spherical representation of this Gaussian diffusion process is provided in Figure 3c.

We use the one-dimensional great-circle summaries for a mixture of two Gaussian diffusions in Figure 3d, where the dominant great circle exhibits a large dynamic range relative to the perpendicular great circles. In fact, one can determine the number of peaks of the diffusion PDF by comparing the dynamic range of the diffusion between the dominant and perpendicular great circles. For a complete picture we also represent the multi-modal diffusion in the (α, β) plane in Figure 3e, where variation is appreciable in both the α and β axes, and on the sphere (Figure 3f).

To overcome the need to compare the variation along the dominant great circle with all perpendicular great circles individually, we define the *average*

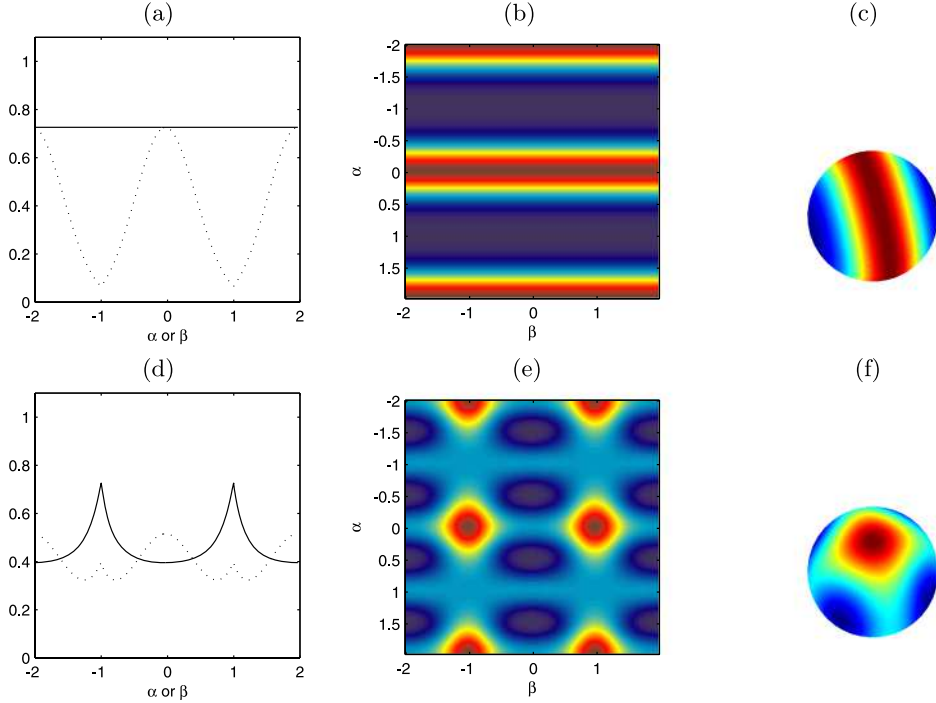


FIG. 3. One- and two-dimensional summaries of Gaussian diffusion processes in q -space, mapped onto the α and β axes (3.1) and their spherical representation. (a, b, c) Prolate diffusion process—eigenvalues ($\lambda_1 \gg \lambda_2 = \lambda_3$). (d, e, f) Mixture of two prolate diffusion processes. The dominant great circle is the solid line in the one-dimensional summaries (a and d), while the dotted line is the diffusion from a single perpendicular great circle for (a) and the average perpendicular diffusion for (d). In the two-dimensional summaries (b and e) all great circles perpendicular to the dominant great circle are plotted on the y -axis to form the (α, β) plane, and the final plots in (c) and (f) show the spherical representation on a single shell in Fourier space, corresponding to a fixed wave number magnitude.

perpendicular diffusion via

$$(3.4) \quad \mathcal{A}_\perp(\alpha) = \frac{1}{2\pi} \int_0^{2\pi} \mathcal{A}(\mathbf{q}_\perp(\alpha, \beta(\vartheta))) d\vartheta,$$

with $\beta(\vartheta) = \cos(\vartheta)$ for $\vartheta \in [0, \pi]$ and $\beta(\vartheta) = -\cos(\vartheta) - 2\text{sgn}[\cos(\vartheta)]$ defining $\beta(\vartheta)$ for $\vartheta \in [0, 2\pi]$. One may also define the average perpendicular diffusion over a half circle by prespecifying a fixed location on the dominant great circle and integrating in a window size ± 1 around this location. This will prevent certain features being masked by the Hermitian symmetry of the q -space measurements. If $\mathcal{A}(\mathbf{q})$ satisfies (2.2), then we have

$$\mathcal{A}_\perp(\alpha) = \frac{1}{2\pi} \int_0^{2\pi} B((\lambda_1 \alpha^2 + (1 - \alpha^2)[\lambda_2 \|\mathbf{q}(\beta(\vartheta))^T \mathbf{v}_2\|^2$$

$$(3.5) \quad + \lambda_3 \|\mathbf{q}(\beta(\vartheta))^T \mathbf{v}_3\|^2)^{1/2} d\vartheta.$$

Thus, we are averaging the density function over small circles parallel to the dominant great circle and $\mathcal{A}_\perp(\alpha)$ measures the average diffusion at a given value of α . In the special case of $\lambda_2 = \lambda_3$, then

$$(3.6) \quad \mathcal{A}_\perp(\alpha) = \frac{1}{2\pi} \int_0^{2\pi} B(\sqrt{\lambda_1 \alpha^2 + \lambda_2 [1 - \alpha^2]}) d\vartheta$$

$$(3.7) \quad = B(\sqrt{\lambda_1 \alpha^2 + \lambda_2 [1 - \alpha^2]}).$$

The average perpendicular diffusion $\mathcal{A}_\perp(\alpha)$ provides a useful summary of variation perpendicular to the dominant great circle. We define a summary of the diffusion PDF via

$$(3.8) \quad \tau = \left[\frac{\max_\alpha \{\mathcal{A}_\perp(\alpha)\}}{\min_\alpha \{\mathcal{A}_\perp(\alpha)\}} \right] / \left[\frac{\max_\beta \{\mathcal{A}(\mathbf{q}_\perp(0, \beta))\}}{\min_\beta \{\mathcal{A}(\mathbf{q}_\perp(0, \beta))\}} \right] - 1.$$

If the diffusion is isotropic, we know that $\lambda_1 = \lambda_2 = \lambda_3$. In this case we have $\mathcal{A}_\perp(\alpha_{\max}) = \mathcal{A}_\perp(\alpha_{\min}) = B(\sqrt{\lambda_1})$ and $\mathcal{A}(\mathbf{q}(0, \beta_{\max})) = \mathcal{A}(\mathbf{q}(0, \beta_{\min})) = B(\sqrt{\lambda_1})$, resulting in $\tau = 0$. If the diffusion is ellipsoidal and $\lambda_2 = \lambda_3$, then $\tau = B(\sqrt{\lambda_2})/B(\sqrt{\lambda_1}) - 1 > 0$. If we adopt the mixture model, with multiple peaks, then it is possible to get $\tau \gg 0$ even if we do not have a single diffusion PDF and we define

$$(3.9) \quad \tilde{\tau} = \min_\beta \max_{\alpha_1, \alpha_2} \left\{ \frac{\mathcal{A}(\mathbf{q}_\perp(\alpha_1, \beta))}{\mathcal{A}(\mathbf{q}_\perp(\alpha_2, \beta))} \right\} / \left[\frac{\mathcal{A}(\mathbf{q}_\perp(0, \beta_{\max}))}{\mathcal{A}(\mathbf{q}_\perp(0, \beta_{\min}))} \right] - 1.$$

We note that under isotropy $\tilde{\tau} \equiv 0$, while if we have a single ellipsoid diffusion $\tilde{\tau} \equiv \tau > 0$. For a double tensor model $\tilde{\tau}$ is more robust and will (in general) take on a lower value compared with τ . In contrast to τ and $\tilde{\tau}$, we could also study the variability in the q -space density directly in terms of the ODF. Tuch (2004), for example, defines the generalized fractional anisotropy (GFA) via

$$(3.10) \quad \text{GFA} = \left\{ \frac{n \sum_{i=1}^n (\text{ODF}_W(\theta_i, \phi_i) - 1/n)^2}{(n-1) \sum_{i=1}^n \text{ODF}_W^2(\theta_i, \phi_i)} \right\}^{1/2},$$

and this measures the nonuniformity of the spatial distribution, as do also the normalized entropy and the nematic order parameter [Tuch (2004)]. While the GFA quantifies the lack of uniformity in the ODF, if there is more than one fiber, determining its statistical properties is nontrivial, unlike the case for τ and $\tilde{\tau}$. Another such measure, generalized anisotropy is defined in terms of the generalized trace of the tensor representation of the mean diffusivity [Özarslan, Vemuri and Mareci (2005)].

3.3. *Measures of anisotropy.* To determine the importance of the identified dominant great circle (or orientation), we can, with a model of (2.2), compare $B(\sqrt{\lambda_1})$ to $B(\sqrt{\lambda_2})$ and $B(\sqrt{\lambda_3})$. We define the following *anisotropy statistic* to perform such a comparison:

$$(3.11) \quad \xi = \frac{\log[\mathcal{A}_\perp(0)]}{\log[\mathcal{A}_\perp(1)]} = \frac{\log[B(\sqrt{\lambda_2})]}{\log[B(\sqrt{\lambda_1})]},$$

where the last equality follows if $\lambda_3 = \lambda_2$. This statistic measures the degree of anisotropy over the q -space shell by comparing the peak-to-trough values (i.e., the value at the maximum great circle, compared to the value at the single point perpendicular to that maximum). Figure 3a displays the difference between the maximum and minimum for an average perpendicular great circle.

The *decay ratio statistic* quantifies the variability of the diffusion over the dominant great circle

$$(3.12) \quad \zeta = \max_{\beta} \frac{\log[\mathcal{A}(\mathbf{q}(\beta))]}{\log[\mathcal{A}(\mathbf{q}(\beta+1))]}.$$

When the two smaller eigenvalues (λ_2 and λ_3) are approximately equal then $\zeta \approx 1$, otherwise $\zeta \gg 1$. The scalene diffusion in Figure 4c and d exhibits such structure ($\zeta \gg 1$).

An indication of forking in white matter would correspond to an asymmetric decay of the diffusion PDF associated with different decays depending on the parity of the deviation. In this case we may no longer model the diffusion PDF as ellipsoidal. For example, in Figure 4a and b we see that while there is still a strong orientation from the dominant great circle, the PDF no longer exhibits symmetric decay away from the dominant great circle. Note that the decay is symmetric in α when averaged over the full sphere to produce $\mathcal{A}_\perp(\alpha)$. Hence, averaging over β is not appropriate if we want to detect asymmetry since a symmetric distribution will be obtained from the Hermitian symmetry of the HARDI measurements when averaging over a full great circle. A suitable *asymmetry statistic* to measure potential asymmetry is given by

$$(3.13) \quad \kappa(\beta) = \frac{(1/2) \int_0^{\pi/2} [\mathcal{A}(\mathbf{q}_\perp(\alpha(\vartheta), \beta)) - \mathcal{A}(\mathbf{q}_\perp(-\alpha(\vartheta), \beta))] d\vartheta}{\int_0^{\pi/2} \mathcal{A}(\mathbf{q}_\perp(\alpha(\vartheta), \beta)) d\vartheta},$$

$$(3.14) \quad \vartheta_{\max} = \arg \max \kappa(\beta(\vartheta)), \quad \beta_{\max} = \beta(\vartheta_{\max}),$$

$$(3.15) \quad \kappa = \frac{2}{\pi} \int_{\vartheta_{\max} - \pi/4}^{\vartheta_{\max} + \pi/4} \kappa(\beta(\vartheta)) d\vartheta.$$

The definition of κ is motivated by the wish to both obtain a test statistic with sufficient power and also to reduce its variance. The discrete approximation to κ will have a smaller variance than $\kappa(\beta_{\max})$. Asymmetry in the

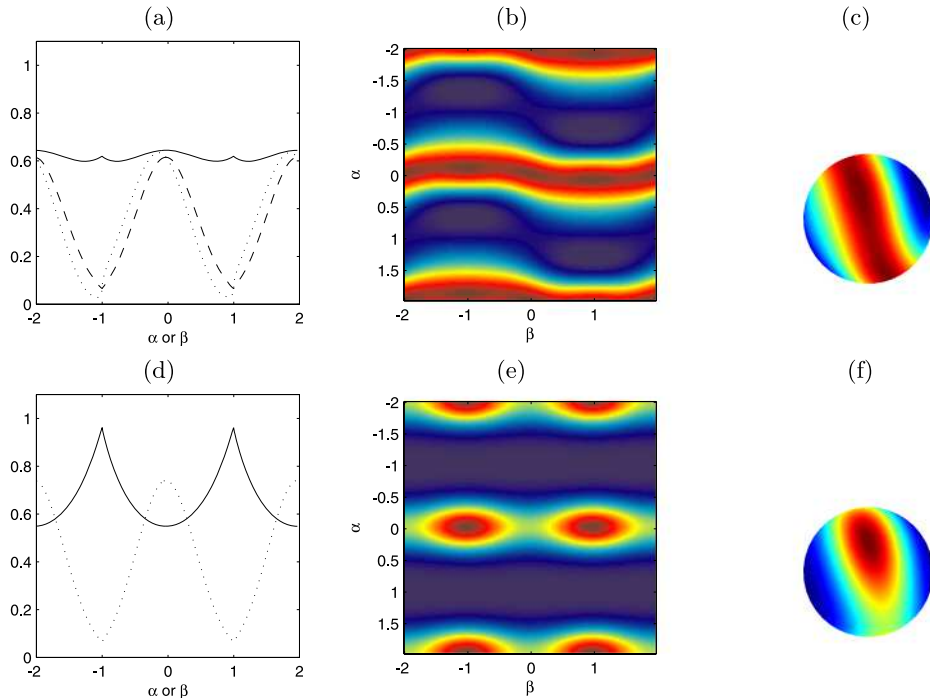


FIG. 4. One- and two-dimensional summaries of Gaussian diffusion processes in q -space, mapped out in the α and β axes (3.1) and their spherical representation. (a, b, c) An asymmetric diffusion process. This is apparent by the asymmetric decay in great circles perpendicular to the dominant great circle in the (α, β) plane. (d, e, f) A scalene diffusion process with eigenvalues $(\lambda_1 \approx \lambda_2 \gg \lambda_3)$. The dominant great circle is the solid line in the one-dimensional summaries (a and d), while the dotted line is the average perpendicular diffusion over $\beta \in [-2, 0]$ for (a) and all β 's for (d). The dashed line in (a) gives the average over all β 's. In the two-dimensional summaries all great circles perpendicular to the dominant great circle are plotted on the y -axis to form the (α, β) plane. The final plots in (c) and (f) show the spherical representation on a single shell in Fourier space, corresponding to a fixed wave number magnitude.

decay from the main peak may occur when the PDF is a mixture of diffusions with varying strengths. If the two populations are sufficiently separated and equivalent in magnitude, then this will be indicated by τ and/or $\tilde{\tau}$ and the diffusion will be recognized as a so-called “crossing fiber.” If the mixture of diffusions contains two different strengths, then the dominating PDF will be recognized when determining \mathbf{x}_{\max} . The remaining structure will not be fully consistent with a single tensor and will (in general) appear to be asymmetric compared to the dominant great circle.

Let us discuss models that will lead to a different structure in the proposed summaries. We refer to Table 1 to summarize the properties of each statistical test, and different diffusion PDFs lead to different structures. It may seem

TABLE 1

The structure of the proposed diffusion models and the representation of their structure in terms of the proposed statistical summaries. Key to abbreviation where the statistics represent N-P/A (non-preference versus anisotropy), C/E (circular versus ellipsoidal), S/A (symmetric versus asymmetric), I/M (isotropic versus multi-modal), M/U (multi-modal versus unimodal)

Hypothesis	Statistic	Isotropic	Prolate	Scalene	Mixture	Heterogeneous
N-P/A	τ	small	large	large	small	large
M/U	$\tilde{\tau}$	small	large	large	small	large
I/M	ξ	one	small	small	small	small
C/E	ζ	–	one	large	–	large
S/A	κ	–	zero	zero	–	large

insufficient to consider only an isotropic PDF, a single peak, a double peak, or something more heterogeneous. However, even with a fully parametric model of a Gaussian DTI framework, a two-tensor model has 13 (identifiable) parameters and a three-tensor model has 19. If one considers acquiring 60 gradient encoding directions (a common sample size), then one is forced to fit a highly-saturated model that results in noisy estimates—especially at higher b -values where the orientational heterogeneity can be well resolved. Pushing much beyond a small number of parameters or features of interest is not advisable with such sampling.

4. Estimation.

4.1. *Parameterizing the (α, β) axes.* Having proposed various summaries of the population of diffusion PDFs at a particular voxel, these must now be estimated from a set of diffusion measurements. The dominant direction may be estimated via

$$\begin{aligned}
 \hat{\mathbf{v}}_1 = \mathbf{x}_{\max} &= \arg \max_{\mathbf{v}, \|\mathbf{v}\|=1} \left\{ \int_{\mathbf{q} \in \mathcal{G}(\mathbf{v})} \hat{\mathcal{A}}(\mathbf{q}) d\mathbf{q} \right\} \\
 (4.1) \qquad &\equiv \arg \max_{\mathbf{x}} \text{FRT}\{\hat{\mathcal{A}}\}(\mathbf{x}),
 \end{aligned}$$

where $\text{FRT}\{\cdot\}$ denotes the Funk–Radon Transform (FRT) as utilized in Tuch (2004). Note that $\hat{\mathcal{A}}(\mathbf{q})$ refers to the multiresolution-based estimator [Olhede and Whitcher (2008a)] and may be replaced by another appropriate estimator. We assume the availability of the quantity $(\hat{\sigma}^*)^2$, an estimator of the variance of the error in $A(\mathbf{q}_k)$ which we define to be σ^2 . The variance of $\hat{\mathcal{A}}(\mathbf{q}_k)$ is assumed to be $\tilde{\sigma}^2 \leq \sigma^2$ and the variance of an interpolated value of the diffusion PDF is $\check{\sigma}^2 \leq \tilde{\sigma}^2 \leq \sigma^2$. The integral may be approximated

numerically by interpolating the observed HARDI measurements at evenly-spaced points along several great circles, each perpendicular to a given \mathbf{x}_i .

The effects of using different numerical methods for this step is a trade-off between increasing numerical accuracy and decreasing variance. Interpolating using spherical harmonics reduces variance but may smooth out details depending on the choice of regularization; see the discussion in Descoteaux et al. (2007) and Hess et al. (2006). We instead use a locally linear interpolation on the polar representation of the observed data that enforces the periodicity of the space in which it was sampled. Simple structures in terms of the observed points can mix over several spherical harmonics, and so the magnitude of individual spherical harmonic coefficients may not be large, even if the local coefficient is large. This fact makes the representation inappropriate for using the smoothing methods of previous authors. The choice of interpolation procedure should be considered in terms of which statistic one is using, as the variance and bias must be balanced specifically for this purpose. We also note that spherical harmonics do not possess the same properties as Fourier vectors, and that an infinite number of harmonics are required for perfect reconstruction of a surface on a sphere, and so any reconstruction from the continuous basis will be inaccurate.

The spatial maximum is determined from $\{\text{FRT}\{\mathcal{A}\}(\mathbf{x}_i)\}_i$. The spatial location \mathbf{x}_{\max} is an estimator of \mathbf{v}_1 and we estimate a vector in the linear subspace spanned by \mathbf{v}_2 and \mathbf{v}_3 from the eigensystem of $\mathbf{I} - \mathbf{x}_{\max}\mathbf{x}_{\max}^T$, this yielding $\hat{\mathbf{v}}_2$ and $\hat{\mathbf{v}}_3$, that maximize the difference in decay in the two axes. For numerical implementation we sample the estimated dominant great circle by discretizing α to $\{\alpha_j\}_{j=1}^N$ and β to $\{\beta_k\}_{k=1}^N$, for an even integer N . A discretized version of (2.15) is then given by

$$(4.2) \quad \hat{\mathbf{q}}_k = \begin{cases} (2 - \beta_k)\hat{\mathbf{v}}_2 \\ \quad - \sqrt{1 - (2 - \beta_k)^2}\hat{\mathbf{v}}_3, & \text{for } k = -N/4, \dots, -1, \\ \beta_k\hat{\mathbf{v}}_2 + \sqrt{1 - \beta_k^2}\hat{\mathbf{v}}_3, & \text{for } k = 0, \dots, N/2 - 1, \\ (-2 - \beta_k)\hat{\mathbf{v}}_2 \\ \quad - \sqrt{1 - (2 + \beta_k)^2}\hat{\mathbf{v}}_3, & \text{for } k = N/2, \dots, 3N/4 - 1, \end{cases}$$

where

$$(4.3) \quad \beta_k = \begin{cases} 2 - \cos(2\pi k/N), & \text{for } k = -N/4, \dots, -1, \\ \cos(2\pi k/N), & \text{for } k = 0, \dots, N/2 - 1, \\ -2 - \cos(2\pi k/N), & \text{for } k = N/2, \dots, 3N/4 - 1. \end{cases}$$

We define $\hat{\mathbf{q}}_k$ for the values of k *not* between $k = -N/4, \dots, 3N/4 - 1$ by cyclically extending (4.2). The choice of discretization guarantees the distance between the orientation associated with a great circle and the great circle is one. The parameters α_j and β_j are individually discretized to force

equal length increments on the great circle. Thus, we discretize the estimated dominant great circle via $\{\hat{\mathbf{q}}_k\}$. Once \mathbf{x}_{\max} has been determined, the diffusion may be characterized directly in q -space. Let us define the sampled great circle vectors for $\{\hat{\mathbf{q}}_k\}$ in (4.2) via

$$(4.4) \quad \hat{\mathbf{q}}_{\perp jk} = \begin{cases} (2 - \alpha_j)\hat{\mathbf{v}}_1 \\ \quad - \sqrt{1 - (2 - \alpha_j)^2}\hat{\mathbf{q}}_k, & \text{for } j = -N/4, \dots, -1, \\ \alpha_j\hat{\mathbf{v}}_1 + \sqrt{1 - \alpha_j^2}\hat{\mathbf{q}}_k, & \text{for } j = 0, \dots, N/2 - 1, \\ (-2 - \alpha_j)\hat{\mathbf{v}}_1 \\ \quad - \sqrt{1 - (2 + \alpha_j)^2}\hat{\mathbf{q}}_k, & \text{for } j = N/2, \dots, 3N/4 - 1; \end{cases}$$

where

$$(4.5) \quad \alpha_j = \begin{cases} 2 - \cos(2\pi j/N), & \text{for } j = -N/4, \dots, -1, \\ \cos(2\pi j/N), & \text{for } j = 0, \dots, N/2 - 1, \\ -2 - \cos(2\pi j/N), & \text{for } j = N/2, \dots, 3N/4 - 1. \end{cases}$$

A discretized version of the average perpendicular diffusion (3.4) is given by $\hat{\mathcal{A}}_{\perp}(\alpha_j) = N^{-1} \sum_k \hat{\mathcal{A}}(\hat{\mathbf{q}}_{\perp jk})$, and we can sum over any N consecutive k (e.g., it does not matter exactly how we sum over k) because of the periodic extension.

4.2. Diagnosing nonuniformity. In order to test large-scale properties of the diffusion directly in q -space, we consider the following statistical hypothesis $H_0: \mathcal{A}(\mathbf{q}) = \mathcal{A} \forall \mathbf{q}$ versus $H_1: \mathcal{A}(\mathbf{q}) = \mathcal{A}_{\mathbb{E}}(\mathbf{q})$. Our test statistic is based on a discretized version of (3.8), given by

$$(4.6) \quad T = \left[\frac{\max_j \{\hat{\mathcal{A}}_{\perp}(\alpha_j)\}}{\min_j \{\mathcal{A}_{\perp}(\alpha_j)\}} \right] / \left[\frac{\max_k \{\mathcal{A}(\hat{\mathbf{q}}_k)\}}{\min_k \{\mathcal{A}(\hat{\mathbf{q}}_k)\}} \right] - 1.$$

The distribution of this test statistic is derived in [Supplementary Material](#). If the observations are isotropic, then the properties along the dominant great circle will be equivalent to the properties on the perpendicular great circle (ignoring any random/discretization errors). The estimators of \mathcal{A} and $\tilde{\sigma}$, under the null of $\hat{\mathcal{A}}(\hat{\mathbf{q}}_k) \cong \mathcal{A} + \tilde{\sigma}\varepsilon$, are given by

$$(4.7) \quad \bar{\mathcal{A}}_N = \frac{1}{N} \sum_{k=1}^N \hat{\mathcal{A}}(\hat{\mathbf{q}}_k) \xrightarrow{N} \frac{1}{2\pi} \int_{\mathcal{G}(\hat{\mathbf{v}}_1)} \mathcal{A}(\mathbf{q}) d\mathbf{q},$$

$$(4.8) \quad \hat{\sigma}_{\mathcal{A}} = \sqrt{\rho} \text{MAD}\{\hat{\mathcal{A}}(\hat{\mathbf{q}}_k) - \bar{\mathcal{A}}_N : k = 1, \dots, N\},$$

where $0 < \rho \leq 3$, $\hat{\mathbf{q}}_k$ defined by (4.2) and $\text{MAD}\{\cdot\}$ is the maximum absolute deviation. These equations provide estimators of the mean value of the isotropic diffusion and the standard deviation of $\hat{\mathcal{A}}(\mathbf{q})$ at the observed

measurements. The parameter ρ is a constant depending on the linear interpolation method used for the implementation. Taking a value of $\rho = 3$ is suitable for our choice of numerical interpolation and we define

$$(4.9) \quad U = T \frac{\bar{\mathcal{A}}_N}{\hat{\sigma}_{\mathcal{A}}}.$$

We can compute the critical value u_α using the fact that $F_U(u_\alpha) = 1 - \alpha$, where $F_U(\cdot)$ is defined in [Supplementary Material](#). We report two critical values here, $u_{0.05} = 0.1185$ for the m which is consistent with our sampling scheme, and $u_{0.05}^{(\text{con})} = 1.9637$ with a conservative distribution approximation.

We also develop a new test based on a null of a multi-modal diffusion, where we define multi-modal in terms of $(\tilde{\mathcal{A}}_{\max} \mathcal{A}_{\min}) / (\tilde{\mathcal{A}}_{\min} \mathcal{A}_{\max}) < c = 2$, where $\tilde{\mathcal{A}}_{\max}$ and $\tilde{\mathcal{A}}_{\min}$ are the maximum and minimum on the perpendicular great circle minimizing (3.9) in β , respectively, while \mathcal{A}_{\max} and \mathcal{A}_{\min} are the maximum and minimum on the dominant great circle. The value of c is fairly arbitrary, but to develop a powerful method of separating the clearly unimodal from the multi-modal, some level must be chosen based on the deterministic structure of the sampled diffusion PDF. To separate unimodal from multi-modal PDFs, we start from $\tilde{\tau}$ and define

$$(4.10) \quad \tilde{T} = \min_k \left\{ \max_{j_1, j_2} \left\{ \frac{\hat{\mathcal{A}}(\hat{\mathbf{q}}_{\perp j_1 k})}{\hat{\mathcal{A}}(\hat{\mathbf{q}}_{\perp j_2 k})} \right\} \right\} / \left[\frac{\max_k \{\hat{\mathcal{A}}(\hat{\mathbf{q}}_k)\}}{\min_k \{\mathcal{A}(\hat{\mathbf{q}}_k)\}} \right] - 1.$$

We shall now choose to distinguish the multi-modal from the unimodal, and so normalize the statistic using $\tilde{U} = (\tilde{T} - [c - 1]) \hat{\mathcal{A}}_{\min} / (\hat{\sigma}_{\mathcal{A}} \sqrt{2c^2 + 2})$, where $\hat{\mathcal{A}}_{\min} = \hat{\mathcal{A}}(\hat{\mathbf{v}}_1)$. The distribution of this test statistic is derived in [Supplementary Material](#), under the specified null hypothesis.

If, on the other hand, we have failed to reject the null hypothesis “ $\mathcal{A}(\mathbf{q}_{\perp}(\alpha, \beta))$ equally variable in β for $\alpha = 0$ as it is in α for a fixed β ,” then based on the T -statistic we need to distinguish voxels that indicate two fiber populations versus isotropic voxels. Let us define a discrete version of (3.11) to be

$$(4.11) \quad X = \frac{\log[\hat{\mathcal{A}}_{\perp}(0)]}{\log[\hat{\mathcal{A}}_{\perp}(1)]}.$$

We can interpret ξ , and the sample version X , as the degree of anisotropy from the average perpendicular great circle. We recognize that the statistic X is comparing the average apparent diffusion coefficient (ADC) on the great circle to the average ADC perpendicular to the great circle, or that (4.11) may be rewritten in terms of the ADC at a fixed value of b via

$$(4.12) \quad X = \sum_k \hat{C}(\hat{\mathbf{q}}_k) / \sum_k \hat{C}(\hat{\mathbf{q}}_{\perp N/4k}).$$

The ADC is $\widehat{C}(\tilde{\mathbf{q}}_j) = -b^{-1} \log A(\tilde{\mathbf{q}}_j)$, for a defined set of \mathbf{q} vectors $\tilde{\mathbf{q}}_j$ [Alexander, Barker and Arridge (2002)]. With an assumption of ellipsoidal structure (2.2) we have averaged the ADC to reduce variance when estimating ξ without accruing bias. We define X_k as the sample anisotropy calculated using only the k th perpendicular great circle via

$$(4.13) \quad X_k = \frac{\log[\widehat{\mathcal{A}}(\hat{\mathbf{q}}_k)]}{\log[\widehat{\mathcal{A}}(\hat{\mathbf{q}}_{\perp N/4k})]},$$

and refer to (4.4) for the definition of $\hat{\mathbf{q}}_{\perp jk}$. Under moderate-to-high SNR X_k may be approximated by a Gaussian random variable. We quantify uncertainty, when there are potentially several peaks, using $\hat{\sigma}_2 = \min\{\hat{\sigma}_{\mathcal{A}}, \hat{\sigma}^*\}$, where $\hat{\sigma}_{\mathcal{A}}$ is defined in (4.7) and $\hat{\sigma}^*$ is the available estimator for σ . By using the minimum, we ensure that the estimated variance is not inflated compared to its pre-smoothing value.

For those voxels where isotropy cannot be rejected, we may now distinguish between isotropy and a multiple-tensor model using X . The *multi-modality* statistic is given by

$$(4.14) \quad Q = \frac{\rho(X - 1)}{\hat{\sigma}_2} |\overline{\mathcal{A}}_N \log \overline{\mathcal{A}}_N|.$$

So we consider the test $H_0: \mathcal{A}(\mathbf{q}) = \mathcal{A} \ \forall \mathbf{q}$ versus $H_1: \max_k \{\mathcal{A}(\mathbf{q}_k)\} \gg \min_k \{\mathcal{A}(\mathbf{q}_k)\}$ (multiple peaks) and use Q as the test statistic, whose distribution under the null is provided in [Supplementary Material](#). The three tests outlined here allow one to at a single voxel diagnose the structure of the diffusion PDF, where U is used to separate anisotropic PDFs from isotropic PDFs, \tilde{U} is used to separate ellipsoid PDFs from multi-modal PDFs and Q is used to separate multi-modal PDFs from isotropic PDFs.

4.3. Diagnosing asymmetry. Having established methodology to discriminate the number of peaks in the diffusion PDF at a single voxel, we now provide additional methodology to characterize the diffusion PDF as scalene versus other forms of asymmetry, for example, to observe the indication of forking or fanning white-matter structure. Let us define

$$(4.15) \quad k_{\max} = \arg \max_{1 \leq k \leq N/4} \frac{\log \widehat{\mathcal{A}}(\hat{\mathbf{q}}_k)}{\log \widehat{\mathcal{A}}(\hat{\mathbf{q}}_{k+N/4})}.$$

The effective degrees of freedom parameters (m, m') are related via $m < m' < 2m$, for robustness, so that

$$(4.16) \quad Z = \frac{\log \widehat{\mathcal{A}}(\hat{\mathbf{q}}_{k_{\max} + N/(2m')})}{\log \widehat{\mathcal{A}}(\hat{\mathbf{q}}_{k_{\max} + N/(2m') + N/4})}.$$

We remark that Z is related in some sense to X_k (refer to Figures 3 and 4). The statistic X_k compares the value of the diffusion PDF at location k on the dominant great circle ($\alpha = 0$) to the value at the perpendicular to the dominant great circle ($\alpha \neq 0$). The statistic Z in contrast looks at the difference in values of the diffusion PDF on the great circle itself ($\alpha = 0$ and β varies). Under the null hypothesis $\mathcal{A}(\cdot)$ is constant on the great circle, and if the medium and minor eigenvalues are approximately equal, then $E\{Z\} = \zeta \approx 1$, otherwise $\zeta \gg 1$. A normalized version of the decay ratio statistic (4.16) is given by

$$(4.17) \quad V = \frac{(Z - 1)|\bar{\mathcal{A}}_N \log \bar{\mathcal{A}}_N|}{\hat{\sigma}_2}.$$

A suitable threshold for this statistic may be found in [Supplementary Material](#). The statistics Q and V , used to test different hypotheses of nonisotropic decay, have similar forms.

The summary statistic κ in (3.15) allows one to diagnose white-matter microstructure that is not consistent with a single ellipsoid diffusion. Departures from such a single ellipsoid diffusion model may be attributed to partial-volume effects, or a heterogeneous population of fibers [Behrens et al. (2007)]. For such a model (2.2) is no longer appropriate and we would rather fit a mixture model with unequal populations—or possibly $\mathcal{A}_{DE}(\cdot)$. In such circumstances one cannot use the average perpendicular great circle to uncover asymmetry since averaging over all possible β 's will produce a symmetric distribution regardless of the underlying fiber characteristics. Taking $\check{k}_{\max} = \arg \max_k \{P_k\}$, we define the *asymmetry statistic* via

$$(4.18) \quad K = \frac{1}{N/4 + 1} \sum_{k=\check{k}_{\max}-N/8}^{\check{k}_{\max}+N/8} P_k,$$

$$(4.19) \quad P_k = \frac{8 \sum_{j=1}^{N/4-1} [\hat{\mathcal{A}}(\hat{\mathbf{q}}_{\perp jk}) - \hat{\mathcal{A}}(\hat{\mathbf{q}}_{\perp (j+N/4)k})]}{\sum_{j=1}^N \hat{\mathcal{A}}(\hat{\mathbf{q}}_{\perp jk})}.$$

Full details on the distribution of K may be found in [Supplementary Material](#). We have chosen $N/8$ to improve the power, since averaging decreases the variance, but the asymmetry is greatest near the maximum (compare with Figure 4b). For tests at a specific voxel we perform the hypothesis test $H_0 : \kappa = 0$ versus $H_1 : \kappa \neq 0$, using quantiles from the standard Gaussian PDF $\phi(\cdot)$. This text identifies diffusion PDFs that are non-Gaussian in terms of the parity structure in the principal axes. However, it does not compare the maximum and minimum of a perpendicular great circle, rather it finds a set of perpendicular great circles for which the decay around the dominant great circle is asymmetric and estimates this average asymmetry, for example, Figure 4b.

The usage of the statistics is now combined at a voxel level. The most important step is to classify the voxel as isotropic, unimodal or multi-modal. With this information the local structure of the peaks in the diffusion PDF may be further characterized. This is similar to the situation when comparing PDFs between voxels for fiber tracking (tractography) where the number of mixture components in the voxels is the first priority and then the components in the diffusion PDF are matched between voxels using local characteristics corresponding to structures at fine scales. From knowledge of white-matter structure one would anticipate varying values of asymmetry before a forking fiber structure, and this would allow us to smoothly go between single voxels with unimodal diffusion to mixtures. These topics shall be discussed in subsequent sections.

4.4. *Example: Crossing and forking fibers.* We consider two typical heterogeneous white-matter structures, a crossing fiber and a forking fiber (Figure 5). The spatial representation of the forking fiber is provided in the first row of the figure, denoted by (i), while the q -space representation of the forking fiber is given on the second row of the figure, denoted by (ii). In the spatial representation we see a single fiber population in voxel (i,a) and, as

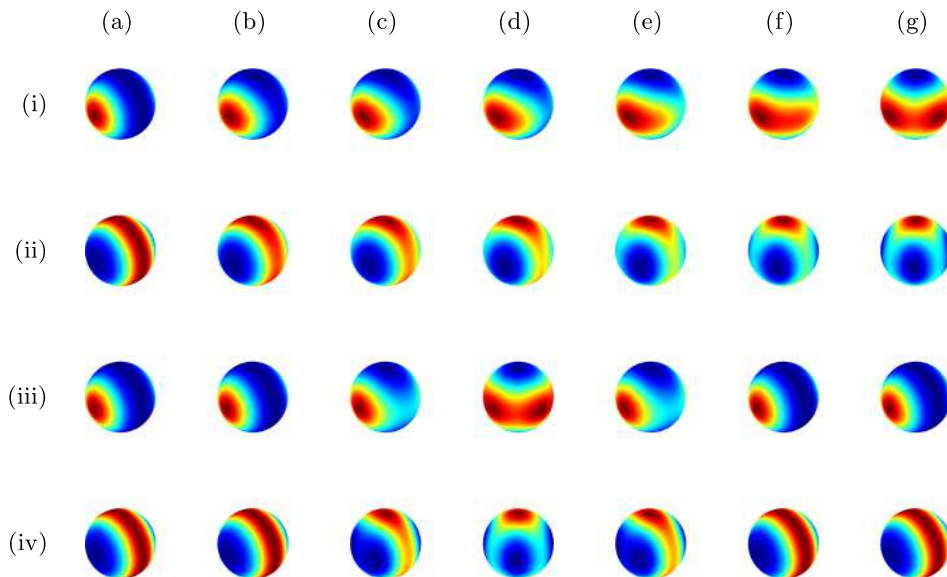


FIG. 5. An illustration of the evolution of a diffusion PDF through a number of adjacent voxels in space and q -space. The first and second rows are the spatial and q -space evolution, respectively, of the diffusion PDF for a forking fiber. The third and fourth rows are the spatial and q -space evolution, respectively, of the diffusion PDF for a crossing fiber. The aim of the plots is to show the changing q -space structure over this evolution.

we traverse from left-to-right, the two populations become more apparent until a second fiber appears in voxel (i,g). The q -space version of these two populations shows a scalene distribution developing in voxels (ii,b)–(ii,e). As the forking progresses, from left-to-right, it appears both highly warped and scalene until the distribution clearly displays multiple fibers in voxel (iii,g). These fibers were generated by aggregating two densities via

$$(4.20) \quad \begin{aligned} \mathcal{A}(\mathbf{q}, t) &= a_1(t)\mathcal{A}_g(\mathbf{q}; \mathbf{\Lambda}^{(1)}(t), \mathbf{\Upsilon}^{(1)}(t)) \\ &+ (1 - a_1(t))\mathcal{A}_g(\mathbf{q}; \mathbf{\Lambda}^{(2)}(t), \mathbf{\Upsilon}^{(2)}(t)). \end{aligned}$$

In the case of the forking fiber, $a_1(t) = 1 - t/2$ and the main directions of $\mathbf{\Upsilon}^{(1)}(t)$ and $\mathbf{\Upsilon}^{(2)}(t)$ are given by $(1, 0, 0)$ and $(\cos(\pi t/2), \sin(\pi t/2), 0)$, respectively. The individual tensors take values similar to $\mathcal{A}_1(\mathbf{q})$ and $t \in [0, 1]$. The spatial representation of the crossing fiber is the third row (iii) of Figure 5, with its corresponding q -space representation in the fourth row (iv). The ellipsoid appears prolate in voxel (iii,a), then two fiber populations are present in voxel (iii,d) and eventually the fiber population returns to a prolate shape. With respect to the parameterization of the crossing fiber in (4.20), $a_1(t) \in \{1, 0.75, 0.5\}$ and the two fibers cross at 90 degrees with parameters similar to $\mathcal{A}_1(\mathbf{q})$.

The description of a crossing fiber is in many ways simpler than a forking fiber. Table 2 lists the summary statistics $(\tau, \tilde{\tau}, \xi, \zeta, \kappa)$ for the crossing and

TABLE 2

Discretized summaries based on nonparametric measures of symmetry for a modeled forking and crossing fiber, compare with Table 1. The summaries show how the statistics evolve over a sequence of voxels undergoing forking or crossing

Forking fiber							
Statistic	(i,a)	(i,b)	(i,c)	(i,d)	(i,e)	(i,f)	(i,g)
τ	10.18	5.12	3.35	1.86	0.82	0.07	−0.14
$\tilde{\tau}$	8.98	4.94	3.36	2.13	1.19	0.33	−0.07
ξ	0.12	0.18	0.21	0.27	0.35	0.53	0.69
ζ	1.03	1.51	1.72	1.91	2.06	2.21	2.67
κ	−0.01	0.03	0.17	0.35	0.45	0.54	0.30
Crossing fiber							
Statistic	(iii,a)	(iii,b)	(iii,c)	(iii,d)	(iii,e)	(iii,f)	
τ	9.19	9.19	1.15	−0.14	1.15	9.19	
$\tilde{\tau}$	8.98	8.98	1.26	−0.07	1.26	8.98	
ξ	0.12	0.12	0.32	0.69	0.32	0.12	
ζ	1.04	1.04	1.74	2.67	1.74	1.04	
κ	0.00	0.00	0.09	0.30	0.09	0.00	

forking fiber examples in Figure 5. Note that these deterministic summaries have not been normalized, unlike the statistics in Section 4 (since there is no noise with which to compare). The mixture of populations of unequal strength in the forking fiber shows a number of characteristics not found in the crossing fiber. For example, the forking fiber is clearly diagnosed as a single population until voxels (i,e)–(i,g), where there is increasing heterogeneity in the fiber population. This is exhibited by increasing values for the decay ratio ζ -statistic, and the asymmetry κ -statistic. For the crossing fiber, we clearly detect the multiple-fiber population in voxel (iii,d) using either the τ or $\tilde{\tau}$ statistics. The multiple-fiber characteristics in the forking example are more complex, where the second fiber population is initially dominated by the first. If we examine the crossing fiber more closely, there is little apparent asymmetry and we can compare the asymmetry statistic, where $\kappa \approx 0$ versus $0.15 \leq \kappa \leq 0.45$ for voxels (i,c)–(i,e). To distinguish multiple fibers from uniformity, we observe that $\xi < 1$, which is the expected value under the hypothesis of isotropy.

5. Simulation study. We illustrate the properties of the proposed q -space summary statistics for the diffusion PDF on a variety of simulated diffusion processes. The following six models attempt to cover common, and not so common, diffusion processes that include both unimodal and multiple tensors:

$$\begin{aligned}
 \mathcal{A}_i(\mathbf{q}) &= \exp(-t\mathbf{q}^T \tilde{\mathbf{D}}_i \mathbf{q}), \quad i = 1, 2, 3, \\
 \tilde{\mathbf{D}}_1 &= 68\tilde{\mathbf{e}}_1\tilde{\mathbf{e}}_1^T + 8\tilde{\mathbf{e}}_2\tilde{\mathbf{e}}_2^T + 8\tilde{\mathbf{e}}_3\tilde{\mathbf{e}}_3^T, \\
 \tilde{\mathbf{D}}_2 &= 68\tilde{\mathbf{e}}_1\tilde{\mathbf{e}}_1^T + 15\tilde{\mathbf{e}}_2\tilde{\mathbf{e}}_2^T + \tilde{\mathbf{e}}_3\tilde{\mathbf{e}}_3^T, \\
 \tilde{\mathbf{D}}_3 &= 28\tilde{\mathbf{e}}_1\tilde{\mathbf{e}}_1^T + 28\tilde{\mathbf{e}}_2\tilde{\mathbf{e}}_2^T + 28\tilde{\mathbf{e}}_3\tilde{\mathbf{e}}_3^T,
 \end{aligned}
 \tag{5.1}$$

$$\begin{aligned}
 \mathcal{A}_4(\mathbf{q}) &= 0.5 \exp(-t\mathbf{q}^T \tilde{\mathbf{D}}_1 \mathbf{q}) + 0.5 \exp(-t\mathbf{q}^T \tilde{\mathbf{D}}_4 \mathbf{q}), \\
 \tilde{\mathbf{D}}_4 &= 68\tilde{\mathbf{e}}_2\tilde{\mathbf{e}}_2^T + 8\tilde{\mathbf{e}}_1\tilde{\mathbf{e}}_1^T + 8\tilde{\mathbf{e}}_3\tilde{\mathbf{e}}_3^T,
 \end{aligned}
 \tag{5.2}$$

$$\begin{aligned}
 \mathcal{A}_5(\mathbf{q}) &= \exp(-11t|\mathbf{q}^T \tilde{\mathbf{e}}_2|^2) \\
 &\times |\exp(-68t|\mathbf{q}^T \tilde{\mathbf{e}}_1|^2) \times [\exp(-0.2t|\mathbf{q}^T \tilde{\mathbf{e}}_3|^2) + \exp(-35t|\mathbf{q}^T \tilde{\mathbf{e}}_3|^2)] \\
 &+ \frac{4}{\pi} D(\sqrt{68t}\mathbf{q}^T \tilde{\mathbf{e}}_1) [D(\sqrt{35t}\mathbf{q}^T \tilde{\mathbf{e}}_3) - D(\sqrt{0.2t}\mathbf{q}^T \tilde{\mathbf{e}}_3)],
 \end{aligned}
 \tag{5.3}$$

$$\begin{aligned}
 \mathcal{A}_6(\mathbf{q}) &= 0.3 \exp(-t\mathbf{q}^T \tilde{\mathbf{D}}_1 \mathbf{q}) + 0.7 \exp(-t\mathbf{q}^T \tilde{\mathbf{D}}_5 \mathbf{q}), \\
 \tilde{\mathbf{D}}_5 &= 42.5\check{\mathbf{e}}_1\check{\mathbf{e}}_1^T + 14\check{\mathbf{e}}_2\check{\mathbf{e}}_2^T + 20\check{\mathbf{e}}_3\check{\mathbf{e}}_3^T,
 \end{aligned}
 \tag{5.4}$$

where $D(x) = \exp(-x^2) \int_0^x \exp(t^2) dt$ is the Dawson function [Abramowitz and Stegun (1972)]. We define $\tilde{\mathbf{e}}_j = \mathcal{R}\mathbf{e}_j$, where the matrix \mathcal{R} rotates the axes $(\mathbf{e}_1, \mathbf{e}_2, \mathbf{e}_3)$ to a new coordinate system $(\tilde{\mathbf{e}}_1, \tilde{\mathbf{e}}_2, \tilde{\mathbf{e}}_3)$. This extra step is added to protect against systematic bias in our estimation procedure due to the diffusion PDF coinciding with the sampling grid. In $\mathcal{A}_6(\mathbf{q})$ this rotation is not implemented, but $(\check{\mathbf{e}}_1, \check{\mathbf{e}}_2, \check{\mathbf{e}}_3)$ has been rotated with respect to $(\mathbf{e}_1, \mathbf{e}_2, \mathbf{e}_3)$ to produce an asymmetric diffusion in the multi-tensor model.

These diffusion processes are displayed in both spatial and frequency domains in Figure 2, where $\mathcal{A}_1(\cdot)$ is a prolate diffusion model (a and g), $\mathcal{A}_2(\cdot)$ is a scalene diffusion (b and h), $\mathcal{A}_4(\cdot)$ is a mixture of two crossing fibers (c and i), $\mathcal{A}_6(\cdot)$ is the first asymmetric diffusion (d and j), and $\mathcal{A}_5(\cdot)$ is the second asymmetric diffusion (e and k). For completeness an isotropic diffusion model $\mathcal{A}_3(\cdot)$ is shown in Figure 2f and l.

We have chosen to define $\tilde{\mathbf{D}}_i = 4 \times 10^{10} \mathbf{D}_i$, $i = 1, \dots, 4$, and normalized $\|\mathbf{q}\| = 1$. With $t = 0.04$ this corresponds to $b = 4t \times 10^{10} = 1600$ s/mm² and the trace of the first three nonnormalized matrices \mathbf{D}_i as 2.1×10^{-9} m²/s [Alexander (2005)]. The function $\mathcal{A}_5(\mathbf{q})$ is obtained from the magnitude of the FT of an asymmetrically decaying diffusion process in space. We illustrate a range of behavior for the scalar statistics defined in q -space using these test functions, providing only a subset in order to compare and contrast their performance. We simulate 1000 realizations for each test function and add Gaussian noise with standard deviation of $\mathcal{A}(0)/2$, $\mathcal{A}(0)/10$, $\mathcal{A}(0)/20$ and $\mathcal{A}(0)/30$ to both the real and imaginary channels using a 60-direction HARDI sampling scheme.

Results, provided in Table 3, are consistent with varying degrees of the SNR. The prolate diffusion \mathcal{A}_1 is clearly detectable, down to an SNR = 1/10, despite using nonparametric methods via the U -statistic. Detecting the scalene diffusion depends on the SNR, while the isotropic diffusion is clearly distinguishable from its alternatives under the full range of SNR using the U -statistics. The multi-tensor diffusion \mathcal{A}_4 is difficult to classify using the U -statistics and its correct classification depends on how well the location of the dominant peak is estimated. If the dominant peak is well determined, then the U -statistic clearly recognizes the density as anisotropic, if not, the q -space measurements are characterized as non-Gaussian instead of multi-modal. If one was only concerned with empirically separating prolate diffusion PDFs from multi-modal diffusion PDFs, rather than performing a hypothesis test, then this would be relatively straightforward, for example, retaining 95% of the unimodal Gaussian with the SNR = 1/20 leads to rejecting all but 11% of the multi-tensor realizations (see the \tilde{U} -statistic). Since we are interested in detecting ellipsoidal decay around a single direction, the variation over the dominant great circle will be large for anisotropic voxels with ellipsoidal decay as well as for multi-modal diffusion PDFs. At an SNR = 1/20 the \tilde{U} -statistic provides complimentary information by strongly

TABLE 3

Hypothesis tests for the six diffusion processes $\{\mathcal{A}_i\}_{i=1}^6$, specified in (5.1), where the number of rejected hypothesis are provided as a single number out of 1000 tests, or as a fraction if fewer than 1000 tests were performed. The nominal size of the tests is 5% for U , V and Q , while the nominal size is 10% for K and \tilde{U} . The hypothesis tests have been carried out at different SNRs, where the noise standard deviation is increasing as you go further down the entries $\text{SNR} \in \{1/30, 1/20, 1/10, 1/2\}$. Keys to the abbreviations are N-P/A (nonpreference versus anisotropy), C/E (circular versus ellipsoidal), S/A (symmetric versus asymmetric), I/M (isotropic versus multi-modal) and M/U (multi-modal versus unimodal)

H_0/H_1	Statistic	\mathcal{A}_1	\mathcal{A}_2	\mathcal{A}_3	\mathcal{A}_4	\mathcal{A}_5	\mathcal{A}_6
SNR = 1/30							
N-P/A	U	1000	988	26	492	1000	802
C/E	V	146/1000	924/988	0/26	382/492	120/1000	495/802
S/A	K	191/1000	108/988	10/26	258/492	491/1000	208/802
I/M	Q	0/0	12/12	21/974	420/508	0/0	195/198
M/U	\tilde{U}	991/1000	136/988	0/26	239/492	996/1000	19/802
SNR = 1/20							
N-P/A	U	1000	855	26	484	1000	727
C/E	V	153/1000	794/855	0/26	338/484	148/1000	267/727
S/A	K	148/1000	38/855	10/26	199/484	331/1000	136/727
I/M	Q	0/0	0/145	23/974	259/516	0/0	201/273
M/U	\tilde{U}	945/1000	46/805	0/23	151/484	942/1000	8/727
SNR = 1/10							
N-P/A	U	1000	239	34	441	998	457
C/E	V	225/1000	214/239	0/34	192/441	194/998	58/457
S/A	K	89/1000	1/239	10/34	99/441	139/998	74/457
I/M	Q	0/0	449/761	20/966	20/539	1/2	18/543
M/U	\tilde{U}	239/1000	7/239	0/34	27/441	174/998	4/457
SNR = 1/2							
N-P/A	U	45	21	25	31	37	24
C/E	V	2/45	2/21	5/25	6/31	4/37	4/24
S/A	K	5/45	4/21	2/25	1/31	4/37	3/24
I/M	Q	1/955	3/979	2/975	2/969	4/963	5/976
M/U	\tilde{U}	2/45	0/21	1/25	0/31	5/37	1/24

separating the prolate (94% rejected) from the multi-tensor model (15.1% rejected, near the nominal value of 10%), but fails to distinguish between the scalene and the multi-tensor models (Table 3). The highly scalene diffusion is mistaken (not surprisingly) for a multi-modal diffusion and such structure may be approximated using two tensors, especially when sparsely sampled on the sphere.

The two distributions with constant behavior on the dominant great circle are not diagnosed with asymmetric decay, while the null hypothesis is rejected for \mathcal{A}_2 in a substantial number of cases in Table 3. The misdiagnosed

multi-modal diffusion PDF \mathcal{A}_4 also has the null hypothesis of multimodality rejected for a substantial number of cases. This is to be expected since the observed diffusion will experience considerable variation over the dominant great circle, consistent with observing a diffusion process with a single dominant direction and ellipsoidal decay.

We fail to reject the null hypothesis of symmetry for the two diffusion processes that are symmetric (\mathcal{A}_1 and \mathcal{A}_2) in most cases, while we reject a larger proportion for \mathcal{A}_5 . There is unfortunately a lack of power in this test which is due to sampling 60 directions, limiting the performance of the test statistic. For \mathcal{A}_6 and keeping the $\text{SNR} = 1/20$, we reject the null hypothesis 38.9% with 60 directions. For \mathcal{A}_5 we reject the null 51.6% of the time using 245 directions at $\text{SNR} = 1/20$ —a clear increase from 35.2% with 60 directions. Increasing the SNR also increases our power to detect such asymmetry, as shown in Table 3. The power of the test improves as the number of directions increase or the amount of asymmetry (better characterized with better spherical sampling) increases. For all of the structural tests performed here there is a direct similarity in effect of increasing the number of grid points to improve the size of the mean under the alternative hypothesis or directly decreasing the variance. This is because as the mean of the alternative hypothesis increases with improved sampling of q -space, this has the same effect as increasing the SNR, as the test statistics are (approximately) functions of their ratio. This direct exchangeability of sampling in frequency versus SNR holds until the distributional approximations break down because of poor resolution in q -space or a diminished signal-to-noise ratio.

6. Analysis of clinical data. HARDI data were acquired from one normal subject (30 year old, male Caucasian) in a Siemens TIM Trio 3.0 Tesla scanner using a 32-channel head coil. Measurement of 64 gradient directions ($b = 1600 \text{ s/mm}^2$) and one T2 image ($b = 0$) were obtained using a twice-refocused diffusion preparation. The slice prescription was 64 slices acquired in the AC-PC plane, $\text{TE} = 95 \text{ ms}$, $\text{FoV} = 240 \times 240 \text{ mm}$, base resolution = 128×128 , slice thickness of 1.9 mm and cardiac gating was applied.

Regions of interest (ROIs) from two slices of the clinical data are provided to illustrate the statistical summaries developed in this paper. Slice 1 contains an ROI that is dominated by single-fiber voxels containing structures such as the corpus callosum and cingulum. Figure 6a shows the voxels using the common color-coding convention [i.e., RGB for the (x, y, z) coordinates] weighted by the estimated fractional anisotropy (FA) at each voxel. The FA for the ROI is reproduced in Figure 6b along with the p -values for the anisotropy and ellipsoidality statistics in Figure 6c and d, respectively. We select a very liberal threshold ($p = 0.15$) for the purpose of exploratory data analysis, not confirmatory data analysis. We observe very few voxels

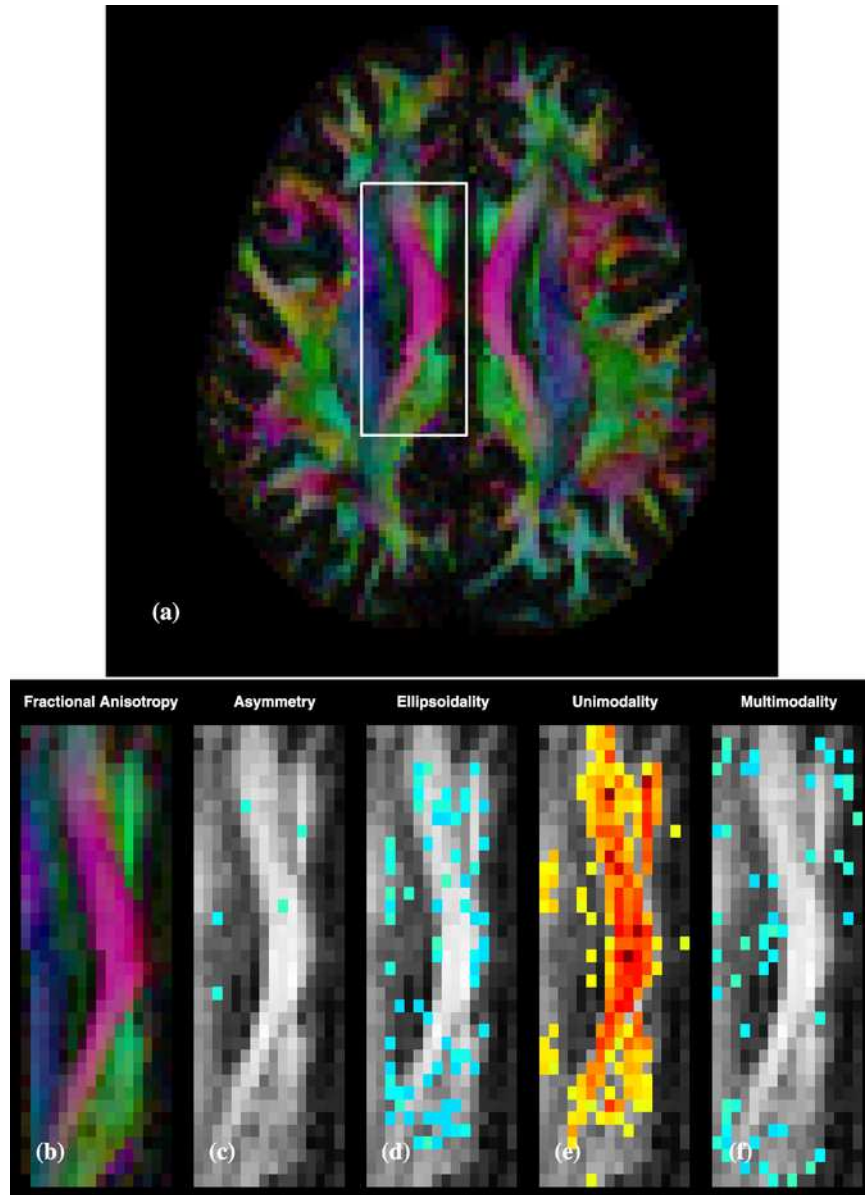


FIG. 6. Axial slice from clinical HARDI acquisition. Color-coded fractional anisotropy (FA) for the whole slice is displayed in (a) along with the boundaries for the ROI (Regions of interest). For the zoomed-in ROI: color-coded FA (b), anisotropy p -values (c), ellipsoidality p -values (d), unimodality test statistic (e) and multimodality p -values (f).

that indicate asymmetry at specific voxels, while the ellipsoidality p -values indicate quite a few voxels that exhibit prolate diffusion. These voxels are located at the borders of strongly directional structures such as the corpus callosum and cingulum, and reaffirm the results obtained in the simulation studies. Additional information about the structure is obtained by plotting the test statistic for unimodality and the p -values from the multi-modality test statistic in Figure 6e and f, respectively. The corpus callosum, and to a lesser extent the cingulum, produce large values in the unimodality test statistic as to be expected from those structures. Multimodality is detected in voxels with reduced FA and/or on the edges of prominent white-matter structures. The pattern of multi-modal voxels identified in Figure 6f in general do not appear to overlap with those voxels that were identified using the ellipsoidality statistic, providing evidence that this methodology is detecting distinct features in the white-matter microstructure.

The ROI selected in slice 2 captures more complicated interactions between white-matter structures such as the corticopontine tract, anterior thalamic radiation and corpus callosum (Figure 7a). The FA for the ROI is reproduced in Figure 7b along with the p -values for the anisotropy and ellipsoidality statistics in Figure 7c and d, respectively. Asymmetry is difficult to detect in these data, but ellipsoidality is quite apparent along the boundaries of the corpus callosum and around the projections into gray matter. The test statistic for unimodality in Figure 7e complement the ellipsoidality results quite well, picking out dominant prolate diffusion (e.g., the voxels dominated by the corpus callosum and to a lesser degree the cingulum) around which the ellipsoidality measure is finding more complex voxels. Finally, the test statistic for multimodality in Figure 7f clearly identifies voxels where the three dominant white-matter structures in this ROI converge, and all other statistics fail to detect any specific structure. The statistical summaries developed here provide complementary information about white-matter microstructure in clinically acquired data.

We focus on a few specific voxels in Figure 7 using the Funk–Radon Transform (FRT) without smoothing. As recommended by Tuch (2004), we have taken the standardized raw FRT to the power five to emphasize structure in the display. Figure 8a and b show the two most anterior voxels that are plotted in Figure 7 (indicated by yellow dots). This tract appears to be “bending” as we move from anterior to posterior, indicated by the shift in direction of the dominant direction seen in the FRTs. The statistics quantify this behavior; the p -values for asymmetry are 0.14 and 0.02 respectively (indicating that the posterior-most voxel is bending more). The unimodality of the anterior voxel is seen from the large unimodality statistic in Figure 7e. We then look at a voxel in a more heterogeneous area, where the major fiber tracts appear to merge: the statistics here indicate multi-modality dominates as is seen in Figure 8c and backed up by Figure 7c–f. We observe the most

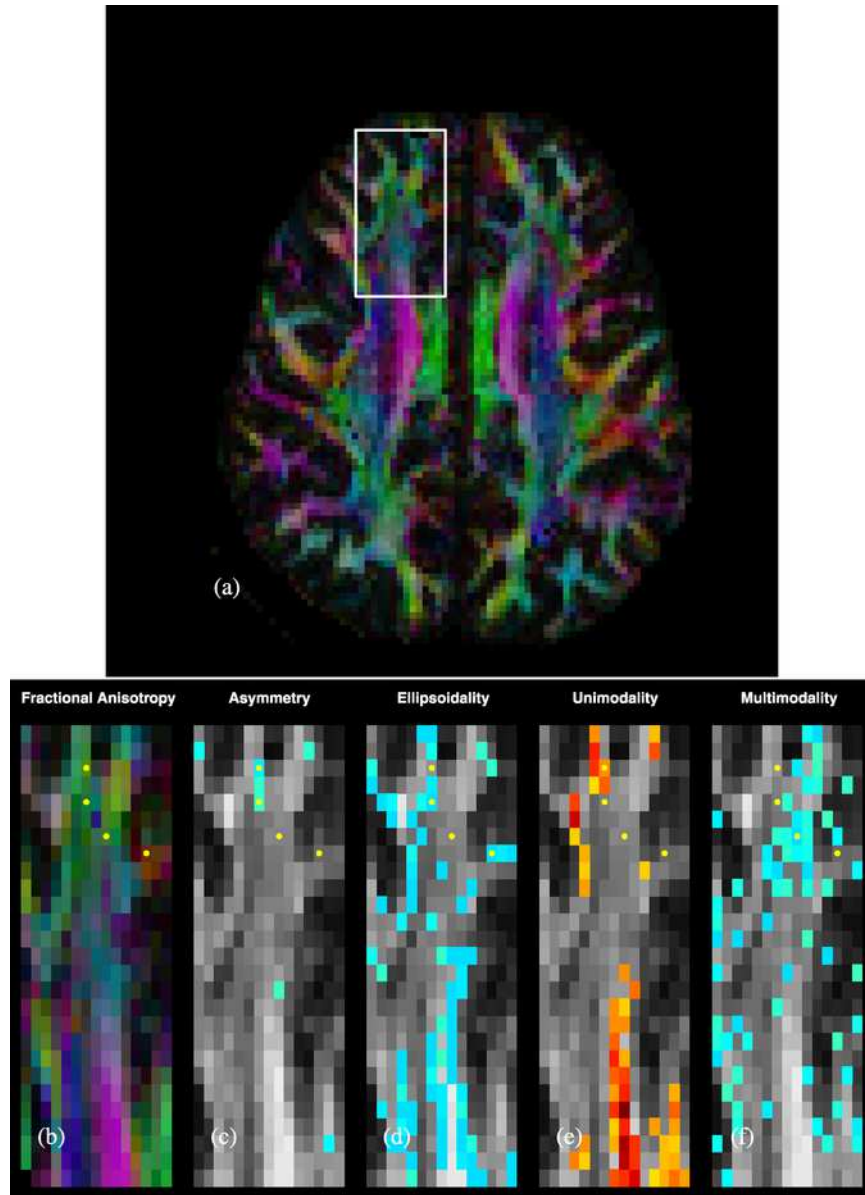


FIG. 7. Axial slice from clinical HARDI acquisition. Color-coded fractional anisotropy (FA) for the whole slice is displayed in (a) along with the boundaries for the ROI. For the zoomed-in ROI: color-coded FA (b), anisotropy p -values (c), ellipsoidal p -values (d), unimodality test statistic (e) and multimodality p -values (f).

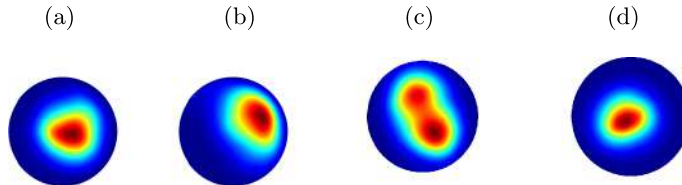


FIG. 8. The raw Funk Radon Transform (FRT) from a collection of voxels indicated by yellow dots in Figure 7. These are plotted in order of decreasing x_2 -coordinate (or going from the top of the image to the bottom). Subplots (a) and (b) both reject the null hypothesis of no asymmetry, with (a) not rejecting prolate diffusion in favor of scalene diffusion. Subplot (c) rejects unimodality in favor of multimodality and also rejects isotropy in favor of multimodality. Subplot (d) is unimodal. The raw FRTs are consistent with these diagnoses.

central voxel has summary statistics that are ellipsoidal but not asymmetric, clearly observed in Figure 8d. The clinical data have provided evidence at a voxel level, backed up by statistical hypothesis testing and observed in the FRT visualizations, that interesting white-matter microstructure may be detected and characterized using the methodology proposed here.

7. Discussion. We have introduced a new set of tools for characterizing orientational structure from HARDI measurements directly in q -space. This methodology is unique when compared with existing methods that rely on reconstructing the spatial information from q -space by different methods of marginalizing the spatial distribution, that is, from calculating a spatial ODF. An ODF has a different meaning if calculated directly from a Gaussian model, from the nonparametric FRT (average orientational distribution over all radii without using the correct volume increment for a marginal PDF) or using PAS-MRI (orientational distribution associated with a single spatial radius or scale). In general, the magnitude associated with an ODF is not comparable between methods, neither is the distribution of noise artifacts. Our methodology is technically linked to the FRT, but unlike the FRT we are not constrained to scalar measures calculated from averages on great circles in q -space, and our methods do not depend on appropriate marginalization to produce summaries. The interpretation of our statistical summaries is straightforward, but we note that in improvements in data acquisition, such as increased sampling of directions.

Most established methods for characterizing features in white-matter microstructure have focused on the problem of determining the number and orientation of peaks in the diffusion PDF. None of the “magnitude” information of these solutions is comparable or indeed interpretable apart from DTI-based models. Savadjiev et al. (2006) have already commented on the unsuitability of such magnitudes as quantitative measures. The problem with

this fact, and the nonlinear transformation often employed for representing q -ball estimates, is that the coherent treatment of noise artifacts becomes much more difficult. The advantage of our theoretical framework, developed for summary statistics, is that we may perform hypothesis tests using critical values that are not functions of unknown parameters. We stress that simulation studies for features of diffusion PDFs are in general misleading unless the proposed summaries are true statistics, that is, their distributions under null hypotheses are parameter independent. For example, critical values determined from Monte Carlo studies for a given diffusion PDF will not (in general) be applicable to other diffusion processes than the simulated process since these critical values are parameter dependent. This can be compared to calculating a simple mean rather than a t -statistic. If we try to elicit the distribution of the sample mean using simulations at fixed variances, then these critical values are only useful for variables with the same variance.

Various nonparametric procedures have been proposed to summarize HARDI data using more than its estimated orientation, for example, by investigating the model order of spherical harmonic decomposition [Frank (2001); Alexander, Barker and Arridge (2002); Descoteaux et al. (2006)]. Chen et al. (2005) modeled the ADC using a product of a truncated spherical harmonics series. In general, an infinite order of spherical harmonic terms must be taken to approximate an arbitrary Gaussian mixture, but they argued that a crossing fiber should be sufficiently reproduced by such a truncated representation and expressed its complexity using the normalized terms in the spherical expansion. Other representations include expressing the ADC in terms of higher-order tensors and spherical harmonics [Descoteaux et al. (2006)], or just via a spherical harmonic representation [Frank (2001)]. Second-order terms in a spherical harmonic decomposition contribute to describing a single-tensor fiber, but more complicated structure must be described in terms of corresponding spatial properties of the PDF directly, rather than the fourth- and higher-order terms which give too much freedom in structure to be a precise tool for the description of fine spatial features. Other measures of the entropy of the diffusion PDF have been proposed by Rao et al. (2004).

Rather than solely focusing only on the number of peaks in the diffusion PDF, we have characterized white-matter microstructure through the diffusion PDF directly in q -space without parametric assumptions or imposing smoothness constraints, as we use a variable bandwidth estimator rather than employing a fixed bandwidth smoother [Olhede and Whitcher (2008a)]. The tissue microstructure is identified as variation in summary statistics that deviate from a simple, symmetric model for the diffusion PDF and is characterized in behavior relative to the identified dominant great circle in q -space. Ellipsoidal diffusion PDFs (2.2) are simple in structure and imply

the existence of a dominant great circle. The deformed ellipsoid class is less stringent in structure, and permits asymmetric decay in minor axes—for example, (2.14)—while still conforming to the existence of a dominant great circle. We describe the precursor to forking structures by either a deformed ellipse or a mixture model, to capture further asymmetric structure. We differentiate between different white-matter microstructure by examining variation over that great circle, or variation perpendicular to the great circle. Allowing for a greater variety of structure in a unidirectional diffusion PDF implies that the power to detect multi-modal diffusion is necessarily reduced compared to using a parametric multi-model model, if the proposed parametric model is correct. We characterized single peak densities by additional summaries, such as the anisotropy statistic, the decay ratio statistic and the asymmetry statistic. The synthetic forking fiber in Figure 5 shows an evolution of such measures as we go between a single fiber and a forking fiber. The synthetic crossing fiber in Figure 5 does not exhibit the same asymmetries.

If one enforces a strict Gaussian (single diffusion tensor) model, then all variation away from symmetry around the dominant direction will be interpreted as evidence for a multi-modal diffusion [Parker and Alexander (2005); Hosey, Williams and Ansoorge (2005); Behrens et al. (2007)]. Modeling using non-Gaussian PDFs allows us to fit asymmetric structure, rather than just the model indicating a lack of fit of a single peak. However, using such models leads to a loss of power if a Gaussian mixture model is appropriate. Caution should be exercised in order to protect against over-interpreting fitted models. With a model that only includes a family of mixtures of Gaussian diffusion processes, one is constrained to estimate a Gaussian mixture, however, for a small number of sampled directions there will inevitably be issues with identifiability. The same realizations may in some cases equivalently be derived from a unimodal diffusion PDF with asymmetric structure or a Gaussian mixture model. If one chooses to select one model rather than the other (i.e., choose an asymmetric and scalene PDF or multiple-tensor), then this decision is based more on the underlying assumptions of the model rather than on the evidence directly provided by the observed data. A large (possibly infinite) collection of Gaussian diffusion processes may be used to approximate an observed set of measurements to an arbitrary accuracy, but one has to consider the possibility that the information being fitted is noise instead of signal. We believe the rule of parsimony should be exercised at all times, and that summaries of orientational structure can be estimated and interpreted in q -space rather than using (potentially) over-parameterized models.

One potential extension to the methods proposed here would be to acquire multiple shells of a fixed radius in q -space instead of typical HARDI sampling [Wu and Alexander (2007); Khachaturian, Wisco and Tuch (2007)], that is, multiple-wavevector or hybrid imaging. In this case the test statistics are

calculated for each shell, and then averaged across the different shells. The dominant orientation would be estimated by a weighted averaging of the estimated dominant orientations for each shell, since its distribution depends on the SNR that is shell-dependent. Another possible acquisition method is diffusion spectrum imaging (DSI), corresponding to a Cartesian sampling of the characteristic function [Wedeen et al. (2005)]. It is more difficult to achieve the same directional resolution in DSI versus multiple-wavevector imaging, and so with realistic sampling times it may not be feasible to perform the same analysis as outlined in this paper. However, other nonparametric summaries could be defined directly in q -space to characterize the spatial properties.

One potential application of these q -space summaries would be to improve fiber-tracking algorithms, similar to the use of the Hessian of a local peak to improve probabilistic tractography models [Seunarine et al. (2007)]. These summaries would be used in addition to directions, to allow more careful tracking through forking and fanning structures (Figure 7), and distinguish local structure more consistently with crossing from such features using both the asymmetry and ellipsoidality measures.

Acknowledgment. The authors thank an anonymous reviewers for a careful reviewing of the paper.

SUPPLEMENTARY MATERIAL

Supplement: Distributions for test statistics

(DOI: [10.1214/10-AOAS441SUPP](https://doi.org/10.1214/10-AOAS441SUPP); .pdf). The supplementary material would be provided at this location.

REFERENCES

- ABRAMOWITZ, M. and STEGUN, I. A. (1972). *Handbook of Mathematical Functions*, 10th ed. Dover, New York.
- ALEXANDER, D. C. (2005). Multiple-fibre reconstruction algorithms for diffusion MRI. *Ann. New York Acad. Sci.* **1046** 113–133.
- ALEXANDER, D. C., BARKER, G. J. and ARRIDGE, S. R. (2002). Detection and modeling of non-Gaussian apparent diffusion coefficient profiles in human brain data. *Magnetic Resonance in Medicine* **48** 331–340.
- BASSER, P. J. (2002). Relationships between diffusion tensor and q -space MRI. *Magnetic Resonance in Medicine* **47** 392–397.
- BASSER, P. J., MATTIELLO, J. and BIHAN, D. L. (1994). Estimation of the effective self-diffusion tensor from the NMR spin-echo. *Journal of Magnetic Resonance B* **103** 247–254.
- BASSER, P. J. and PIERPAOLI, C. (1996). Microstructural and physiological features of tissues elucidated by quantitative-diffusion-tensor MRI. *Journal of Magnetic Resonance B* **111** 209–219.

- BEHRENS, T. E. J., JOHANSEN-BERG, H., JBABDI, S., RUSHWORTH, M. F. S. and WOOLRICH, M. W. (2007). Probabilistic tractography with multiple fibre orientations: What can we gain? *NeuroImage* **34** 1077–1088.
- CALLAGHAN, P. T. (1993). *Principles of Nuclear Magnetic Resonance Microscopy*. Clarendon Press, Oxford.
- CHEN, Y., GUO, W., ZHENG, Q., RAO, M. and LIU, Y. (2005). Apparent diffusion coefficient approximation and diffusion anisotropy characterization in DWI. In *IPMI 2005* 246–257. Springer, Berlin.
- DESCOTEAUX, M., ANGELINO, E., FITZGIBBONS, S. and DERICHE, R. (2006). Apparent diffusion coefficients from high angular resolution diffusion imaging: Estimation and applications. *Magnetic Resonance in Medicine* **56** 395–410.
- DESCOTEAUX, M., ANGELINO, E., FITZGIBBONS, S. and DERICHE, R. (2007). Regularized, fast and robust analytical Q -ball imaging. *Magnetic Resonance in Medicine* **58** 497–510.
- FRANK, L. R. (2001). Characterization of anisotropy in high angular resolution diffusion-weighted MRI. *Magnetic Resonance in Medicine* **45** 935–939.
- GRADSHTEYN, I. S. and RYZHIK, I. M. (2000). *Tables of Integrals, Series and Products*, 6th ed. Academic Press, New York. [MR1773820](#)
- GUDBJARTSSON, H. and PATZ, S. (1995). The Rician distribution of noisy MRI data. *Magnetic Resonance in Medicine* **34** 910–914.
- HESS, C. P., MUKHERJEE, P., HAN, E. T., XU, D. and VIGNERON, D. B. (2006). Q -ball reconstruction of multimodal fibre orientations using the spherical harmonic basis. *Magnetic Resonance in Medicine* **56** 104–117.
- HOSEY, T., WILLIAMS, G. and ANSORGE, R. (2005). Inference of multiple fiber orientations in high angular resolution diffusing imaging. *Magnetic Resonance in Medicine* **54** 1480–1489.
- JANSONS, K. M. and ALEXANDER, D. C. (2003). Persistent angular structure: New insights from diffusion magnetic resonance imaging data. *Inverse Problems* **19** 1031–1046. [MR2024687](#)
- JENSEN, J. H., HELPERN, J. A., RAMANI, A., LU, H. and KACZYNSKI, K. (2005). Diffusional kurtosis imaging: The quantification of non-Gaussian water diffusion by means of magnetic resonance imaging. *Magnetic Resonance in Medicine* **53** 1432–1440.
- JIAN, B. and VEMURI, B. C. (2007). A unified computational framework for deconvolution to reconstruct multiple fibres from diffusion weighted MRI. *IEEE Transactions on Medical Imaging* **26** 1464–1471.
- KADEN, E., KNÖSCHE, T. R. and ANWANDER, A. (2007). Parametric spherical deconvolution: Inferring anatomical connectivity using diffusion MR imaging. *NeuroImage* **37** 474–488.
- KHACHATURIAN, M. H., WISCO, J. J. and TUCH, D. S. (2007). Boosting the sampling efficiency of q -ball imaging using multiple wavevector fusion. *Magnetic Resonance in Medicine* **57** 289–296.
- MATÉRN, B. (1960). Spatial variation. In *Stochastic Models and Their Application to Some Problems in Forest Surveys and Other Sampling Investigations* **39**. Statens Skogsforskningsinstitut, Stockholm, Sweden. [MR0169346](#)
- MORI, S. and VAN ZIJL, C. M. (2002). Fiber tracking: Principles and strategies—a technical review. *NMR in Biomedicine* **15** 468–480.
- OLHEDE, S. C. and WHITCHER, B. (2008a). HARDI wavelet and non-parametric estimation. Technical report, University College London.
- OLHEDE, S. C. and WHITCHER, B. (2008b). A statistical framework to characterise microstructure in high angular resolution diffusion imaging. In *5th IEEE International Symposium on Biomedical Imaging* 899–902. IEEE, Piscataway, New Jersey.

- ÖZARSLAN, E., VEMURI, B. C. and MARECI, T. M. (2005). Generalized scalar measures for diffusion MRI using trace, variance and entropy. *Magnetic Resonance in Medicine* **53** 866–876.
- ÖZARSLAN, E., SHEPHARD, T. M., VEMURI, B. C., BLACKBAND, S. J. and MARECI, T. M. (2006). Resolution of complex tissue microarchitecture using the diffusion orientation transform. *NeuroImage* **31** 1086–1103.
- PARKER, G. J. M. and ALEXANDER, D. C. (2005). Probabilistic anatomical connectivity derived from the microscopic persistent angular structure of cerebral tissue. *Philos. Trans. Royal Soc. London Ser. B* **360** 893–902.
- RAO, M., CHEN, Y., VEMURI, B. C. and WANG, F. (2004). Cumulative residual entropy: A new measure of information. *IEEE Transactions on Information Theory* **50** 1220–1228. [MR2094878](#)
- SAVADJIEV, P., CAMPBELL, J. S. W., PIKE, G. B. and SIDDIQI, K. (2006). 3D curve inference for diffusion MRI regularization and fibre tractography. *Medical Image Analysis* **10** 799–813.
- SEUNARINE, K., COOK, P. A., HALL, M. G., EMBLETON, K. V., PARKER, G. J. M. and ALEXANDER, D. C. (2007). Exploiting peak anisotropy for tracking through complex structure. In *Mathematical Methods in Biomedical Image Analysis 1*. IEEE Computer Society, Rio de Janeiro.
- TOURNIER, J. D., CALAMANTE, F., GADIAN, D. G. and CONNELLY, A. (2004). Direct estimation of the fiber orientation density function from diffusion-weighted MRI data using spherical deconvolution. *NeuroImage* **23** 1176–1185.
- TUCH, D. S. (2004). Q-ball imaging. *Magnetic Resonance in Medicine* **52** 1358–1372.
- TUCH, D. S., REESE, T. G., WIEGELL, M. R., MAKRIS, N., BELLIVEAU, J. W. and WEDEEN, V. J. (2002). High angular resolution diffusion imaging reveals intravoxel white matter fiber heterogeneity. *Magnetic Resonance in Medicine* **48** 577–582.
- WEDEEN, V. J., HAGMANN, P., TSENG, W. Y., REESE, T. G. and WEISSKOFF, R. M. (2005). Mapping complex tissue architecture with diffusion spectrum magnetic resonance imaging. *Magnetic Resonance in Medicine* **54** 1377–1386.
- WU, Y. C. and ALEXANDER, A. L. (2007). Hybrid diffusion imaging. *NeuroImage* **36** 617–629.

DEPARTMENTS OF COMPUTER SCIENCE
AND STATISTICAL SCIENCE
UNIVERSITY COLLEGE LONDON
GOWER STREET
LONDON WC1 E6BT
UNITED KINGDOM
E-MAIL: s.olhede@ucl.ac.uk

GLAXOSMITHKLINE CLINICAL
IMAGING CENTRE
HAMMERSMITH HOSPITAL
IMPERIAL COLLEGE LONDON
DU CANE ROAD
LONDON W12 0HS
UNITED KINGDOM
E-MAIL: brandon.j.whitcher@gsk.com